Research Square

Preprints are preliminary reports that have not undergone peer review.
They should not be considered conclusive, used to inform clinical practice,
or referenced by the media as validated information.

Lattice Distortion and Defect-Associated Functional Properties of $Ba_{1-x}Fe_xCrO_3$ Perovskites: Linking Microstructural Disorder with Optical and Dielectric Responses

Ariful Alam

arifulalam@mbstu.ac.bd

Mawlana Bhashani Science and Technology University

Mst. Sukhi Akter

Mawlana Bhashani Science and Technology University

Shefa Akter

Mawlana Bhashani Science and Technology University

Md. Ridwanul Hasan

Bangladesh Army University of Science and Technology

Md. Abdur Rob

National Institute of Textile Engineering and Research

Jobair Maudood

Bangladesh Atomic Energy Commission

Md. Saiful Islam

Bangladesh Atomic Energy Commission

Nazia Khatun

Bangladesh Council of Scientific and Industrial Research

Ayesha Siddika

Bangladesh Council of Scientific and Industrial Research

Suravi Islam

Bangladesh Council of Scientific and Industrial Research

Abul K. Azad

Universiti Brunei Darussalam

Md. Shah Alam

Shahjalal University of Science and Technology

Shahzad Hossain

Bangladesh Atomic Energy Commission

Research Article

Keywords: Fe doped $BaCrO_3$ perovskite oxide, Functional oxide materials, Defect engineering, Structural characterization, Optical and dielectric properties

Posted Date: November 23rd, 2026

DOI: https://doi.org/10.21203/rs.3.rs-11725699/v1

License: This work is licensed under a Creative Commons Attribution 4.0 International License.
Read Full License

Additional Declarations: No competing interests reported.

Lattice Distortion and Defect-Associated Functional Properties of $Ba_{1-x}Fe_xCrO_3$ Perovskites: Linking Microstructural Disorder with Optical and Dielectric Responses

Ariful Alam[1,2*], Mst. Sukhi Akter[1], Shefa Akter[1], Md. Ridwanul Hasan[3*], Md. Abdur Rob[4], Jobair Maudood[5], Md. Saiful Islam[5], Nazia Khatun[6], Ayesha Siddika[6], Suravi Islam[7], Abul K. Azad[8], Md. Shah Alam[2], Shahzad Hossain[5*]

[1]*Department of Physics, Mawlana Bhashani Science and Technology University, Santosh, Tangail 1902, Bangladesh*

[2]*Department of Physics, Shahjalal University of Science and Technology, Sylhet 3114, Bangladesh*

[3]*Department of Arts & Sciences, Bangladesh Army University of Science and Technology, Saidpur 5310, Bangladesh*

[4]*Department of Computer Science and Engineering, National Institute of Textile Engineering and Research, Savar, Dhaka 1350, Bangladesh*

[5]*Institute of Nuclear Science and Technology, Bangladesh Atomic Energy Commission, GPO Box No. 3787, Dhaka 1000, Bangladesh*

[6]*BCSIR Dhaka Laboratories, Bangladesh Council of Scientific and Industrial Research, Dhaka 1205, Bangladesh*

[7]*Institute of Glass and Ceramic Research & Testing, Bangladesh Council of Scientific and Industrial Research, Dhaka 1205, Bangladesh*

[8]*Faculty of Integrated Technologies, Universiti Brunei Darussalam, Jalan Tungku Link, Gadong 1410, Brunei Darussalam*

***Corresponding authors' Emails:** arifulalam@mbstu.ac.bd, ridwanulhasan11@gmail.com, shahzad_baec@yahoo.com

Abstract

$Ba_{1-x}Fe_xCrO_3$ (x = 0.1–0.4) perovskite ceramics were synthesized by the conventional solid-state route to investigate their composition-dependent structural, optical, dielectric, and electrical properties. X-ray diffraction (XRD) indicated an orthorhombic perovskite framework across the investigated compositions, with no detectable secondary crystalline phases within the measurement limits. Five XRD line-broadening methods yielded model-dependent coherent-domain size estimates of approximately 31–78 nm, highlighting the sensitivity of microstructural parameters to the analytical approach. Complementary FTIR spectra provided supporting information on metal–oxygen lattice vibrations. Tauc analysis showed a decrease in the estimated optical band gap from 3.22 to 2.99 eV with increasing Fe content, indicating a composition-dependent shift in the optical absorption edge. Dielectric measurements revealed frequency-dependent responses, with BFC-1 exhibiting comparatively lower dielectric loss. AC conductivity also varied with composition and frequency, with BFC-3 and BFC-4 showing higher conductivity at high frequencies. A non-monotonic conductivity feature around 1–1.5 MHz was observed, although its underlying mechanism could not be established. Within the adopted structural model, Fe is considered predominantly associated with the Ba/A-site; however, partial B-site incorporation cannot be excluded because direct site-occupancy characterization was not performed. Possible oxygen nonstoichiometry and associated defect contributions remain unverified. Overall, the results reveal composition-dependent correlations among structural, optical, dielectric, and electrical properties while highlighting the need for further structural and transport characterization to clarify the underlying mechanisms.

Keywords: Fe doped $BaCrO_3$ perovskite oxide, Functional oxide materials, Defect engineering, Structural characterization, Optical and dielectric properties.

1. Introduction

Perovskite oxides constitute a highly versatile class of functional materials owing to their exceptional structural flexibility and diverse physical properties, including electronic transport, dielectric response, optical activity, magnetism, and catalytic performance [1,2]. Their general ABO_3 framework can accommodate a wide range of cations at the A- and B-sites, enabling systematic control over crystal symmetry, lattice distortion, defect chemistry, and metal–oxygen interactions [3]. Among transition-metal-based perovskites, barium chromite ($BaCrO_3$) has attracted considerable interest because of its Cr-centered electronic structure, strong metal–oxygen interactions, oxygen-defect chemistry, and potential multifunctional properties [4]. However, the functional characteristics of $BaCrO_3$-based materials are strongly governed by the coupling between structural distortion, defect states, electronic structure, and charge-transport processes.

The physical properties of $BaCrO_3$ are closely associated with its CrO_6 octahedral framework, in which Cr–O–Cr connectivity provides an important pathway for electronic interactions, charge transport, and polarization processes [5,6]. Structural imperfections, including oxygen vacancies and variations in the oxidation state of the transition-metal sublattice, can introduce localized electronic states and substantially modify the optical and electrical responses of the material [7]. While an appropriate concentration of defects may facilitate charge transport and enhance polarization, excessive structural disorder can promote charge trapping, interfacial polarization, dielectric loss, and electrical instability. Consequently, controlled modification of the A-site provides a potentially effective approach for regulating the structural environment and defect chemistry of $BaCrO_3$ while preserving the fundamental Cr-based perovskite framework.

In this context, partial substitution of Ba by Fe in $Ba_{1-x}Fe_xCrO_3$ offers an alternative route for tailoring the structural and functional characteristics of $BaCrO_3$. Fe incorporation is modeled predominantly at the Ba/A-site, based on the nominal composition and the available structural characterization, introduces a difference in ionic size, charge state, and local chemical environment relative to Ba^{2+}, which can generate lattice distortion and modify the structural stability of the perovskite framework [8,9]. Such A-site substitution may influence the geometry and distortion of the CrO_6 octahedral network indirectly through changes in lattice dimensions and local electrostatic interactions. In addition, the charge imbalance associated with Fe incorporation may promote compensating defects, including oxygen vacancies and changes in the oxidation-state distribution of the transition-metal sublattice. These substitution-induced structural and defect modifications can consequently affect crystallite development, lattice strain, optical absorption, dielectric polarization, and charge-transport behavior. Therefore, controlled Fe substitution at the Ba-site represents a potentially useful strategy for engineering the structure–property relationships of $BaCrO_3$-based perovskites [10].

Despite extensive research on transition-metal-containing perovskite oxides, the composition-dependent relationships among Fe incorporation, microstructural evolution, optical response, and dielectric behavior in $Ba_{1-x}Fe_xCrO_3$ remain insufficiently established. In particular, the

combined evolution of crystallite size, lattice strain, metal–oxygen bonding, optical band-gap characteristics, and frequency-dependent dielectric response has not been comprehensively examined across a systematic composition series. Understanding these relationships is important because the functional properties of perovskite oxides depend on the interplay among crystal structure, local bonding, structural disorder, and electronic states.

Previous studies have highlighted the sensitivity of Fe-containing functional oxides to structural characteristics and processing conditions. Karki et al. investigated the relationships among structural, optical, and magnetic properties in brownmillerite $KBiFe_2O_5$-based ceramics, whereas Venkatrao et al. demonstrated the influence of sintering conditions on crystallite size and the optical and magnetic properties of $YFeO_3$ ceramics [11,12]. These findings underscore the importance of correlating structural and microstructural characteristics with functional responses, while leaving the composition-dependent behavior of $Ba_{1-x}Fe_xCrO_3$ to be examined systematically.

Accordingly, this study investigates $Ba_{1-x}Fe_xCrO_3$ (x = 0.1–0.4) using X-ray diffraction (XRD), Fourier-transform infrared (FTIR) spectroscopy, UV–visible spectroscopy, and dielectric characterization. XRD patterns are analyzed using the Debye–Scherrer, Williamson–Hall, Halder–Wagner, and modified Scherrer methods to compare crystallite-size and diffraction-broadening characteristics [13]. FTIR spectroscopy provides complementary information on metal–oxygen vibrations, while UV–visible spectroscopy is used to evaluate composition-dependent optical absorption and Tauc-derived band-gap characteristics. Dielectric measurements are used to examine frequency-dependent polarization and electrical response. By comparing these results across the composition series, this work assesses the correlations among structural and microstructural variations and optical and dielectric behavior. Fe is considered predominantly incorporated at the Ba/A-site within the adopted structural model; however, partial occupancy of the Cr-centered B-site cannot be excluded without direct site-sensitive characterization. The findings provide a basis for evaluating composition-dependent functional responses in $Ba_{1-x}Fe_xCrO_3$ without presuming a unique defect mechanism or a specific device application.

2. Methodology

The perovskite type ceramics materials $Ba_{1-x}Fe_xCrO_3$ with nominal Fe substitution levels of x = 0.1, 0.2, 0.3, and 0.4 were synthesized by the conventional solid-state reaction method (Fig. 1). The samples were designated BFC-1, BFC-2, BFC-3, and BFC-4, respectively. This method was selected because of its simplicity, cost-effectiveness, and suitability for the preparation of crystalline mixed-metal oxide ceramics [14–16].

Barium carbonate ($BaCO_3$, ≥99.8%), iron(III) oxide (Fe_2O_3, ≥97.0%), and chromium(III) oxide (Cr_2O_3, ≥99.9%) were used as starting precursors. The required quantities were calculated according to the nominal stoichiometric compositions of $Ba_{1-x}Fe_xCrO_3$ and accurately weighed using a digital microbalance. Although the precursor purities were not identical, the resulting products exhibited the characteristic reflections of the orthorhombic perovskite phase without detectable secondary crystalline phases within the detection limit of the XRD measurements. The weighed powders were thoroughly mixed and manually ground

in an agate mortar for approximately 40 min using a small amount of ethanol as a liquid grinding medium. The addition of ethanol facilitated homogeneous mixing and intimate contact among the constituent powders. After grinding, the resulting mixture was dried to completely remove the ethanol before proceeding to the subsequent calcination step.

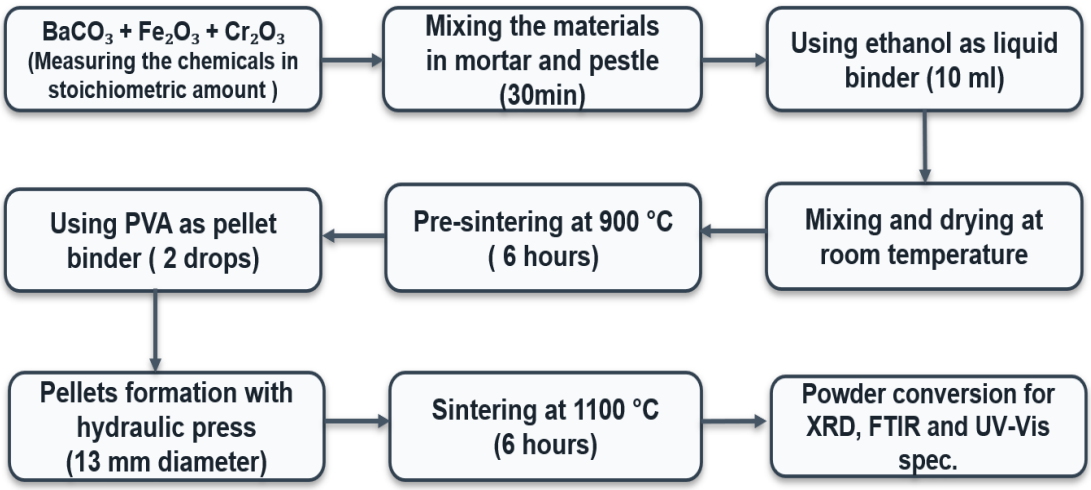

Fig. 1: Workflow diagram for the synthesis of $Ba_{1-x}Fe_xCrO_3$ perovskite ceramics.

The homogenized precursor mixtures were calcined at 900 °C for 6 h in an electric furnace. After natural cooling to room temperature, the powders were reground for 30 min to improve homogeneity and reduce soft agglomerates. Polyvinyl alcohol (PVA) was then added as a temporary binder, followed by an additional 30 min of grinding to ensure uniform distribution.

The powders were uniaxially pressed into circular pellets approximately 13 mm in diameter using a hydraulic press under a load of 3.5 tons. The pellets were subsequently sintered at 1100 °C for 6 h in a muffle furnace to promote crystallization and densification of the $Ba_{1-x}Fe_xCrO_3$ ceramics [17]. After sintering, a portion of each specimen was pulverized for structural, vibrational, and optical characterization, while the remaining pellets were retained for dielectric and electrical measurements [18].

Table 1: Geometrical dimensions, mass, and bulk density of the sintered $Ba_{1-x}Fe_xCrO_3$ ceramics.

Sample	Diameter (mm)	Thickness (mm)	Mass (g)	Bulk density (g cm^{-3})
BFC-1	12.5	2.7	1.4784	4.46
BFC-2	12.4	2.6	1.3237	4.22
BFC-3	12.2	3.2	1.6563	4.43
BFC-4	12.2	2.5	1.2840	4.39

The bulk density of the sintered pellets was calculated from their measured mass and geometrical volume using $\rho = m/[\pi(d/2)^2 t]$, where m, d, and t represent the pellet mass, diameter, and thickness, respectively. All pellets were compacted under a 3.5-ton load and sintered at 1100 °C for 6 h under identical conditions. After sintering and cooling to room temperature, the pellet dimensions and masses were measured for bulk-density determination. The measured densities ranged from 4.22 to 4.46 g cm^{-3}. Although the density variation was non-monotonic with Fe content, the relatively narrow range indicates comparable macroscopic densification among the compositions. Such variation may arise from differences in powder packing, residual porosity, and the extent of densification during sintering rather than from a strictly monotonic dependence on Fe concentration

3. Results and Discussion

3.1 Theoretical Structural Stability Analysis

The synthesized compositions were designated as BFC-1, BFC-2, BFC-3, and BFC-4, corresponding to Fe substitution concentrations of x = 0.1, 0.2, 0.3, and 0.4, respectively. The systematic incorporation of Fe at the Cr-site was performed to investigate its influence on the structural evolution, defect formation, optical characteristics, and dielectric transport behavior of the $BaCrO_3$ perovskite system.

To study the structural stability of the synthesized $Ba_{1-x}Fe_xCrO_3$ perovskites, the Goldschmidt tolerance factor (t) was calculated using the following equation[19,20] :

$$t = \frac{r_A + r_O}{\sqrt{2}(r_B + r_O)} \qquad (1)$$

where r_A, r_B, and r_O represent the ionic radii of the A-site cation, B-site cation, and oxygen ion, respectively. The calculated tolerance factor values are presented in Table 1. For a stable perovskite structure, the tolerance factor generally lies within the range of 0.8–1.0, which indicates a suitable geometric relationship between the A-site cation and the BO_6 octahedral framework [21,22]. The obtained tolerance factor values for all $Ba_{1-x}Fe_xCrO_3$ compositions are within this stability range, confirming the formation of a stable perovskite structure.

The octahedral factor (μ) is defined as the ratio of the ionic radius of the B-site cation to that of the oxygen anion in ABO_3 perovskite systems and is expressed as [23,24]:

$$\mu = r_B / r_O \qquad (2)$$

where r_B represents the ionic radius of the B-site cation and r_O denotes the ionic radius of the oxygen ion (O^{2-}). The octahedral factor (μ) provides a geometrical measure of the suitability of the B-site cation for octahedral coordination in the perovskite framework. For conventional perovskite structures, μ values within the range of approximately 0.414–0.732 are generally associated with stable BO_6 octahedral configurations [25].

Table 2: Goldschmidt tolerance factors and Octahedral factor for $Ba_{1-x}Fe_xCrO_3$

Fe substitution, x	Material composition	Octahedral factor, μ	Goldschmidt tolerance factor, t
0.1	$Ba_{0.9}Fe_{0.1}CrO_3$	0.40	1.06
0.2	$Ba_{0.8}Fe_{0.2}CrO_3$	0.40	1.03
0.3	$Ba_{0.7}Fe_{0.3}CrO_3$	0.41	1.01
0.4	$Ba_{0.6}Fe_{0.4}CrO_3$	0.41	0.98

As shown in Table 2, the calculated octahedral factor ((\mu)) increases slightly from 0.40 to 0.41 with increasing Fe content, whereas the Goldschmidt tolerance factor ((t)) decreases from 1.06 to 0.98. Within the adopted structural model, Fe is considered to occupy predominantly the Ba/A-site; therefore, the observed changes in these geometrical descriptors are not attributed to direct Fe substitution at the Cr/B-site. Instead, they reflect the assumed changes in the effective A-site and B-site ionic radii used in the calculations. The decrease in (t) indicates a progressive change in the geometrical relationship between the A-site cations and the CrO_6 framework. Values approaching and slightly below unity at higher Fe concentrations may suggest a greater tendency toward structural relaxation or octahedral tilting, although these possibilities cannot be established from tolerance-factor calculations alone.

These parameters should be interpreted as geometrical indicators rather than direct evidence of defect concentration, charge compensation, or phase stability. Their composition-dependent variation provides a useful framework for discussing the experimental XRD results, including changes in lattice parameters and microstructural characteristics. Possible implications for metal–oxygen vibrations, optical transitions, dielectric polarization, and charge transport are considered alongside the corresponding experimental results, without assigning a unique microscopic mechanism to the calculated trends.

3.2 X-ray Diffraction Analysis

The X-ray diffraction (XRD) patterns of $Ba_{1-x}Fe_xCrO_3$ (x = 0.1–0.4) were analyzed using Match! Version 4.0 software with reference crystallographic data from the Crystallography Open Database (COD) (Fig. 2). The observed reflections were indexed to an orthorhombic perovskite structure, with the assigned planes (011), (211), (301), (121), (221), (330), (410), (102), (041), (022), (232), (042), (113), and (333). These results support the presence of a predominantly orthorhombic perovskite phase, although minor poorly crystalline or amorphous phases cannot be excluded.

The diffraction patterns exhibit composition-dependent variations in peak intensity and profile, while no clearly resolved systematic shift of the principal reflections is evident. Such observations may be consistent with changes in the average structural environment and

microstructural characteristics; however, they do not independently establish a specific distortion or defect mechanism.

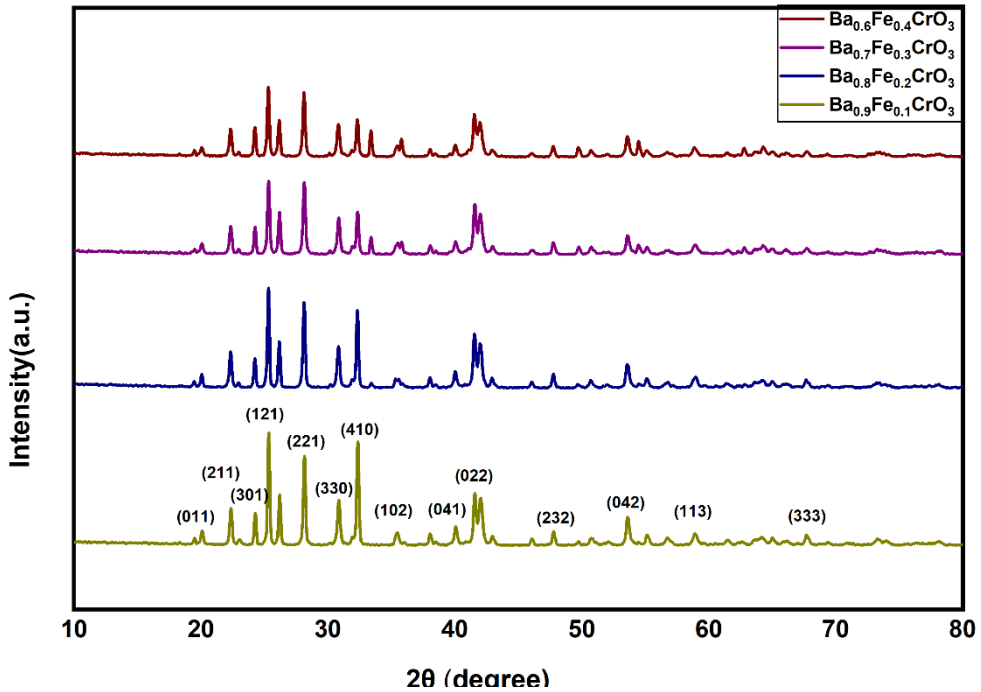

Fig.2: The X-ray diffraction (XRD) patterns of $Ba_{1-x}Fe_xCrO_3$ (x = 0.1–0.4)

The lattice parameters and unit-cell volumes obtained from the indexed XRD patterns are summarized in Table 3. The reported lattice parameters are (a = 16.4494), 11.6107, 9.6312, and 13.6163 Å; (b = 9.7133), 9.4956, 7.0841, and 8.7011 Å; and (c = 4.7531), 7.1219, 6.9844, and 5.1344 Å for (x = 0.1), 0.2, 0.3, and 0.4, respectively. The corresponding unit-cell volumes calculated using (V = abc) are 759.44, 785.19, 476.53, and 608.30 Å^3. These values exhibit substantial non-monotonic variations rather than a simple systematic lattice expansion or contraction.

Table 3: Theoretical and Structural Parameters of $Ba_{1-x}Fe_xCrO_3$ Perovskites.

Material	**Lattice parameters (Å)**			**Phase (α= β= γ=90°)**	**Cell volume (Å^3)**
	a	**b**	**c**		
$Ba_{0.90}Fe_{0.10}CrO_3$	16.4494	9.7133	4.7531	Orthorhombic	759.44
$Ba_{0.80}Fe_{0.20}CrO_3$	11.6107	9.4956	7.1219	Orthorhombic	785.19
$Ba_{0.70}Fe_{0.30}CrO_3$	9.6312	7.0841	6.9844	Orthorhombic	476.53
$Ba_{0.60}Fe_{0.40}CrO_3$	13.6163	8.7011	5.1344	Orthorhombic	608.30

Within the adopted structural model, Fe is considered to be incorporated predominantly at the Ba/A-site. The difference in ionic size and nominal charge between Fe^{3+} and Ba^{2+} could influence the local A-site environment and the geometrical relationship between the A-site cations and the CrO_6 framework. Possible consequences include local lattice relaxation, changes in bond geometry, and modification of the strain state. Nevertheless, these mechanisms cannot be distinguished from the present indexed lattice parameters alone, and the unusually large variations in cell dimensions require particular caution.

Therefore, the XRD results may support the interpretation that Fe incorporation induces composition-dependent modifications of the structural geometry while preserving the orthorhombic perovskite framework across the investigated composition range. Within the adopted structural model, Fe is considered to be incorporated predominantly at the Ba/A-site, where its substantially smaller ionic size and different nominal charge relative to Ba^{2+} introduce A-site size and charge mismatch that can perturb the local lattice geometry, octahedral tilting, and microstrain. The composition-dependent tolerance-factor values, lattice-parameter variations, and XRD line-broadening behavior are consistent with such progressive structural perturbation. However, these observations provide indirect rather than site-specific evidence, and laboratory XRD cannot unambiguously distinguish A- and B-site Fe occupancy in the absence of direct site-sensitive characterization or constrained Rietveld refinement. Therefore, partial Fe incorporation at the Cr-centered B-site cannot be completely excluded, and the predominant A-site incorporation should be regarded as a working structural model rather than definitive evidence of exclusive A-site occupancy. The resulting composition-dependent structural modifications provide an important basis for understanding the subsequent evolution of crystallite size, lattice strain, optical response, dielectric polarization, and charge-transport behavior in $Ba_{1-x}Fe_xCrO_3$.

3.3 Williamson-Hall Analysis for Strain and Crystallite Size Evolution

For the $Ba_{1-x}Fe_xCrO_3$ (x = 0.1–0.4) ceramics materials, the Williamson–Hall method was applied to separate the contributions of crystallite size and lattice strain from the XRD peak broadening [26]. The W–H equation used can be expressed as:

$$\beta\cos\theta = \frac{k\lambda}{D} + 4\epsilon\sin\theta \qquad (3)$$

where β is the full width at half maximum (FWHM) of the diffraction peak, θ is the Bragg angle, λ is the X-ray wavelength, D is the coherent crystallite size, ε is the microstrain, and k is the shape factor. In this representation, plotting βcosθ against 4sinθ gives an intercept related to the coherent-domain size and a slope corresponding to the microstrain within the assumptions of the conventional W–H model [26]. The FWHM values used in the present calculations were determined from the experimentally measured diffraction peaks using Origin and Match! software. A separately measured instrumental-broadening profile was not available; therefore, an independent instrumental-broadening correction was not applied. Consequently, the calculated crystallite-size and microstrain values may contain a contribution from instrumental broadening and should be interpreted as comparative, model-dependent estimates rather than absolute structural parameters.

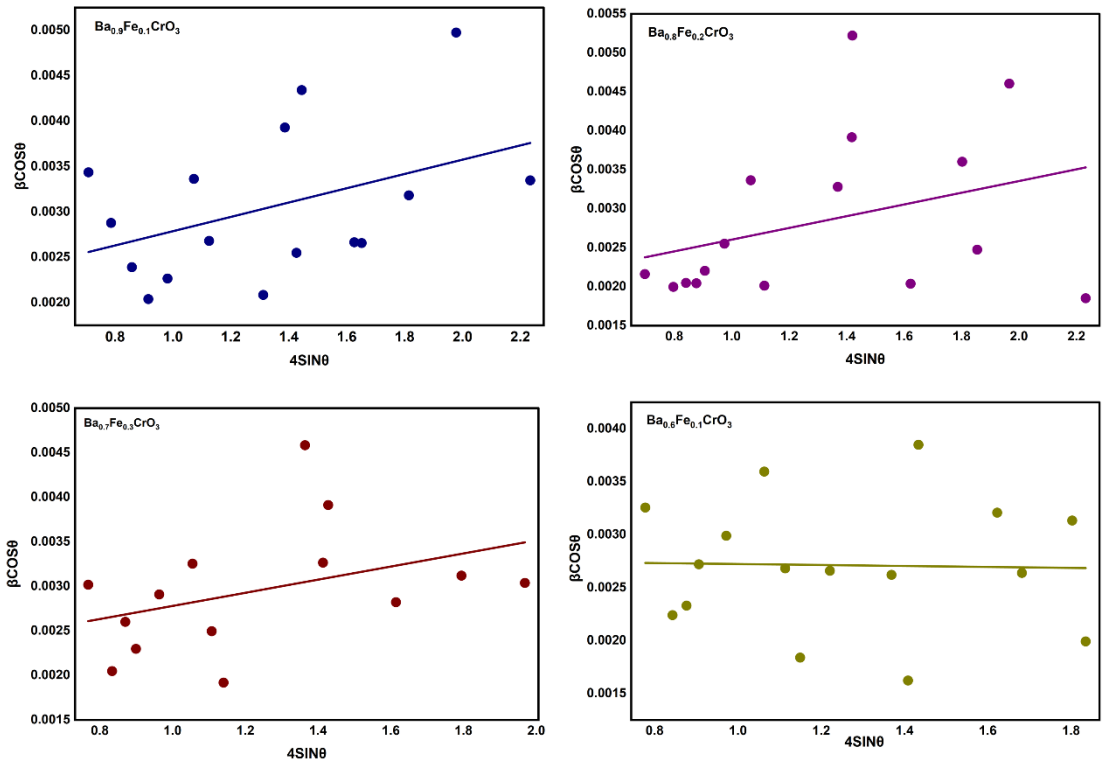

Fig. 3: Williamson-Hall plots to evaluate the contributions of crystallite size and lattice strain

The W–H plots for the investigated compositions (Fig. 3) exhibit approximately linear behavior. The coherent-domain sizes were 72.41, 78.28, 70.99, and 52.28 nm for BFC-1, BFC-2, BFC-3, and BFC-4, respectively. The size initially increased from x = 0.1 to 0.2 and subsequently decreased, with the lowest value observed for BFC-4. This non-monotonic variation may reflect composition-dependent changes in coherent-domain dimensions and strain-related broadening. However, these estimates do not directly establish grain or particle refinement.

The fitted W–H slopes provide corresponding estimates of microstrain. Their variation across the compositions suggests changes in the strain contribution to diffraction-line broadening. BFC-4 exhibits a comparatively reduced slope, indicating a lower fitted microstrain contribution within the adopted model. Although this may be consistent with changes in strain accommodation at higher Fe content, W–H analysis alone cannot establish strain relaxation or identify specific defect mechanisms, including oxygen-vacancy formation. The approximately linear plots support the use of the conventional W–H model as a comparative approach but do not exclude contributions from anisotropic broadening, peak-profile characteristics, or instrumental effects.

3.4 Microstructural Parameter Estimation through Halder–Wagner Analysis

The Halder–Wagner (H–W) method was additionally employed as a complementary line-broadening approach to estimate the coherent crystallite/domain size and lattice strain from the X-ray diffraction peak broadening (Fig. 4). Unlike the conventional Williamson–Hall (W–H) treatment, the H–W approach uses a different mathematical representation of the size- and strain-related contributions to peak broadening [27,28]. Unlike the Williamson–Hall (W–H) method, H–W uses a different mathematical treatment of size- and strain-related broadening; therefore, the two approaches provide complementary, model-dependent estimates rather than independent confirmation of absolute microstructural parameters. The full width at half maximum (FWHM) values were obtained from experimentally measured diffraction peaks using Origin and Match! Version 4.0. Because an independent instrumental-broadening profile was unavailable, no separate instrumental correction was applied. The calculated parameters are consequently interpreted as comparative estimates.

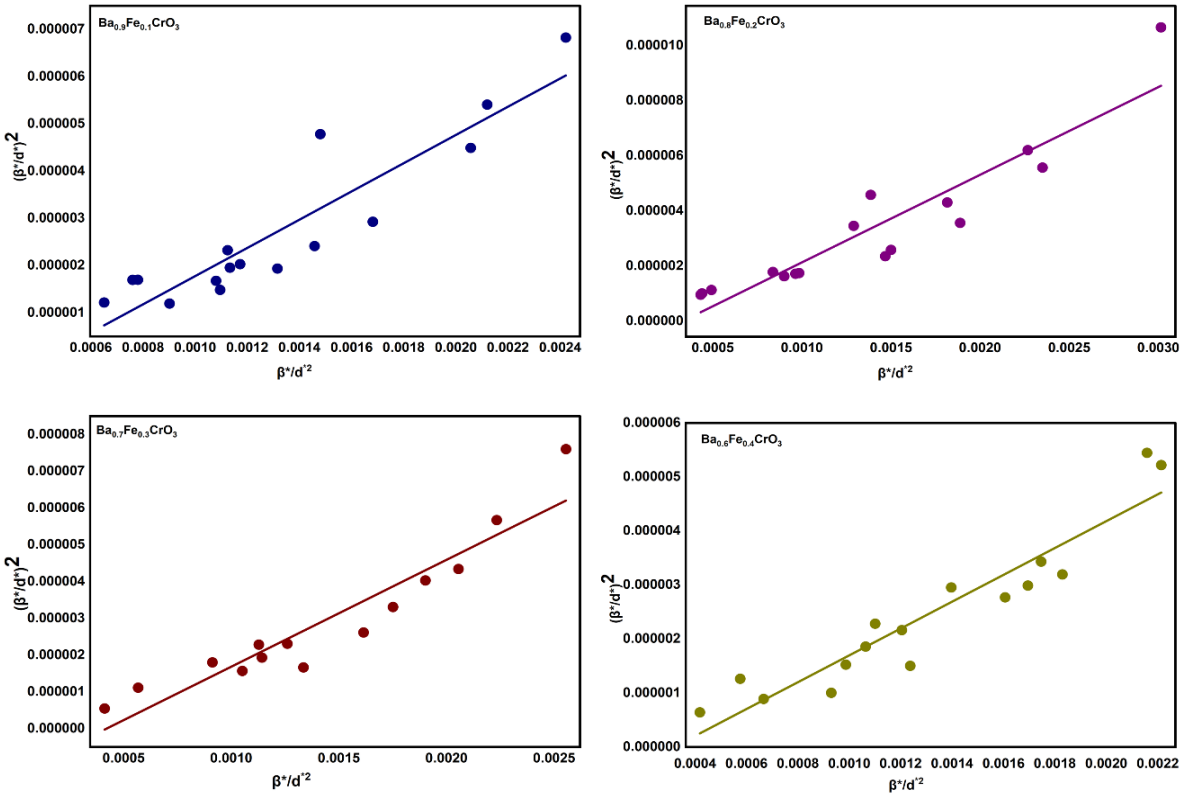

Fig. 4: Halder–Wagner plots to determine crystallite size and lattice strain through integral breadth analysis of X-ray diffraction peaks.

The H–W-derived microstrain values were 0.00299, 0.00318, 0.00291, and 0.00248 for BFC-1, BFC-2, BFC-3, and BFC-4, respectively. The microstrain initially increased from BFC-1 to BFC-2 before decreasing at higher Fe contents. Correspondingly, the estimated crystallite sizes increased to 34.36 and 40.32 nm for BFC-3 and BFC-4, respectively. These results indicate a non-monotonic, composition-dependent relationship between the fitted strain contribution and coherent-domain size. The trend may be consistent with changes in local

structural accommodation as the composition varies; however, the H–W analysis alone cannot establish a specific strain-relaxation mechanism.

Within the adopted structural model, Fe is considered to be predominantly incorporated at the Ba/A-site, potentially modifying the local A-site environment and its coupling with the CrO_6 framework. Such changes may contribute to the observed microstructural trends, although direct site-occupancy evidence and complementary defect-sensitive measurements would be required to establish the underlying mechanisms. Possible charge compensation or oxygen nonstoichiometry cannot be confirmed from the H–W results alone.

The differences between H–W- and W–H-derived crystallite sizes reflect the distinct assumptions and mathematical treatments used by the two methods. Accordingly, the estimates should be interpreted comparatively, with emphasis on composition-dependent variations rather than a single definitive crystallite-size trend. The reported sizes represent XRD-derived coherent diffraction-domain dimensions, not physical grain or particle sizes.

3.5 Modified Scherrer Analysis for Crystallite Size Estimation

The Modified Scherrer (M–S) method was employed as an additional approach for estimating the crystallite size of $Ba_{1-x}Fe_xCrO_3$ (x = 0.1–0.4) while reducing the influence of strain-related peak broadening (shown in Fig. 5). Unlike the conventional Debye–Scherrer treatment, the adopted M–S approach considers the angular dependence of peak broadening through a linear relationship between cosθ and 1/β, providing an alternative estimation of the coherent crystallite dimension in nanocrystalline materials [29,30]. The corresponding M–S plots for BFC-1 to BFC-4 exhibit satisfactory linear fitting, indicating that the diffraction broadening can be described predominantly in terms of finite crystallite size within the adopted model, although residual microstrain may also contribute.

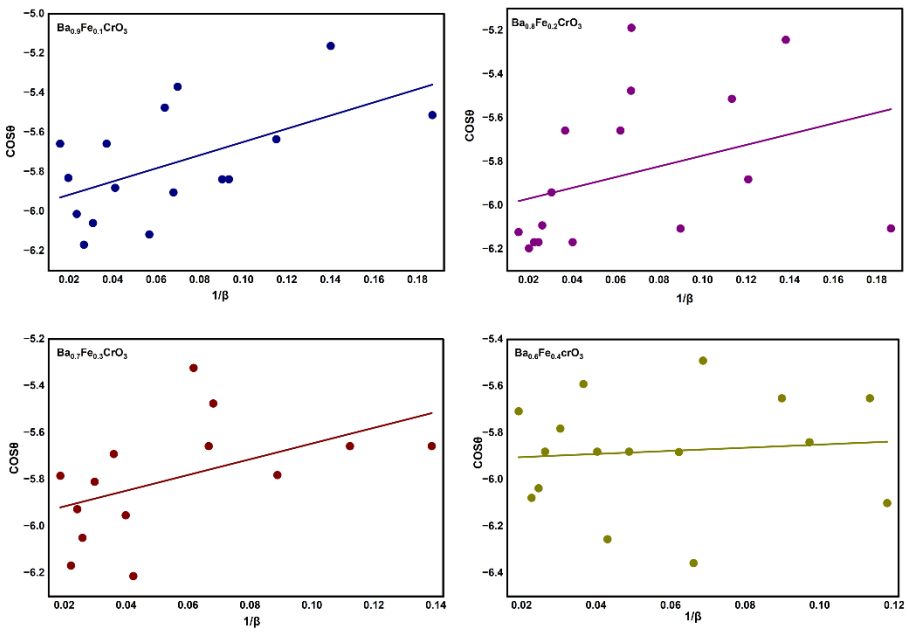

Fig. 5: Modified Scherrer (M–S) plots to estimate crystallite size from X-ray diffraction peak broadening.

The M–S-derived crystallite sizes were 57.43, 59.51, 57.43, and 53.80 nm for BFC-1, BFC-2, BFC-3, and BFC-4, respectively. The corresponding fitted intercepts were −5.98285, −6.01840, −5.98291, and −5.91761. The estimated size increased slightly from BFC-1 to BFC-2 and subsequently decreased, indicating a non-monotonic composition dependence. Although this variation may reflect changes in coherent-domain development and local structural accommodation, the M–S results alone cannot establish a specific mechanism involving structural relaxation, substitution-induced disorder, or charge compensation.

Within the adopted structural model, Fe is considered to be predominantly incorporated at the Ba/A-site, potentially modifying the local A-site environment and its coupling with the CrO_6 framework. Such modifications may contribute to the observed microstructural trends; however, the M–S analysis does not directly establish cation-site occupancy, oxygen-vacancy concentration, or defect redistribution.

The M–S estimates differ from those obtained using the Williamson–Hall, Halder–Wagner, Debye–Scherrer, and size–strain plot approaches because the methods employ different mathematical treatments and assumptions. Accordingly, the M–S values are best interpreted as complementary estimates rather than definitive crystallite sizes. Overall, the results indicate modest, non-monotonic variations in XRD-derived coherent-domain size across the investigated compositions. These estimates provide a comparative basis for examining composition-dependent microstructural changes alongside the optical, dielectric, and electrical results.

3.6 Crystallite Size Evolution with Debye–Scherrer Analysis

The crystallite sizes estimated using the Debye–Scherrer equation for $Ba_{1-x}Fe_xCrO_3$ (BFC-1 to BFC-4) are 50.52, 56.69, 51.68, and 56.35 nm, respectively. Thus, all compositions exhibit coherent crystallite dimensions within the nanocrystalline range of approximately 50–57 nm. The relatively narrow variation indicates that progressive Fe substitution produces only moderate changes in the average coherent crystallite size rather than a fundamental alteration of the crystallization behavior [31].

The variations may be associated with changes in the local structural environment and strain-related broadening accompanying Fe incorporation. However, the D–S method does not independently separate size- and strain-related contributions; therefore, the calculated values should be interpreted as approximate, model-dependent estimates rather than definitive crystallite dimensions.

The D–S estimates complement those obtained using the Williamson–Hall, Halder–Wagner, modified Scherrer, and size–strain plot methods. Differences among the calculated values are expected because the approaches use different assumptions to analyze diffraction-line broadening. Collectively, the results indicate composition-dependent variations in XRD-derived coherent-domain size while retaining dimensions within the nanometer scale. These

estimates provide a comparative basis for examining the relationship between microstructural variation and the optical, dielectric, and electrical responses of $Ba_{1-x}Fe_xCrO_3$.

3.7 Size-Strain Plot (SSP) Method

The SSP analysis reveals a non-monotonic variation in crystallite size with increasing Fe substitution (Fig. 6). The crystallite sizes of BFC1, BFC2, BFC3, and BFC4 were estimated to be 44.70, 64.65, 50.64, and 45.26 nm, respectively. The crystallite size increased markedly from 44.70 nm for BFC1 (x = 0.10) to a maximum of 64.65 nm for BFC2 (x = 0.20), suggesting that this composition provides comparatively favorable conditions for coherent crystallite growth. With further Fe incorporation, the crystallite size decreased to 50.64 nm for BFC3 and 45.26 nm for BFC4. This subsequent reduction may be associated with enhanced lattice distortion, compositional disorder, and defect-related effects arising from progressive Fe substitution, which can hinder the growth of coherently diffracting domains. Overall, the crystallite-size sequence follows BFC2 > BFC3 > BFC4 > BFC1, demonstrating a distinct composition-dependent evolution of the coherent diffraction domains [32].

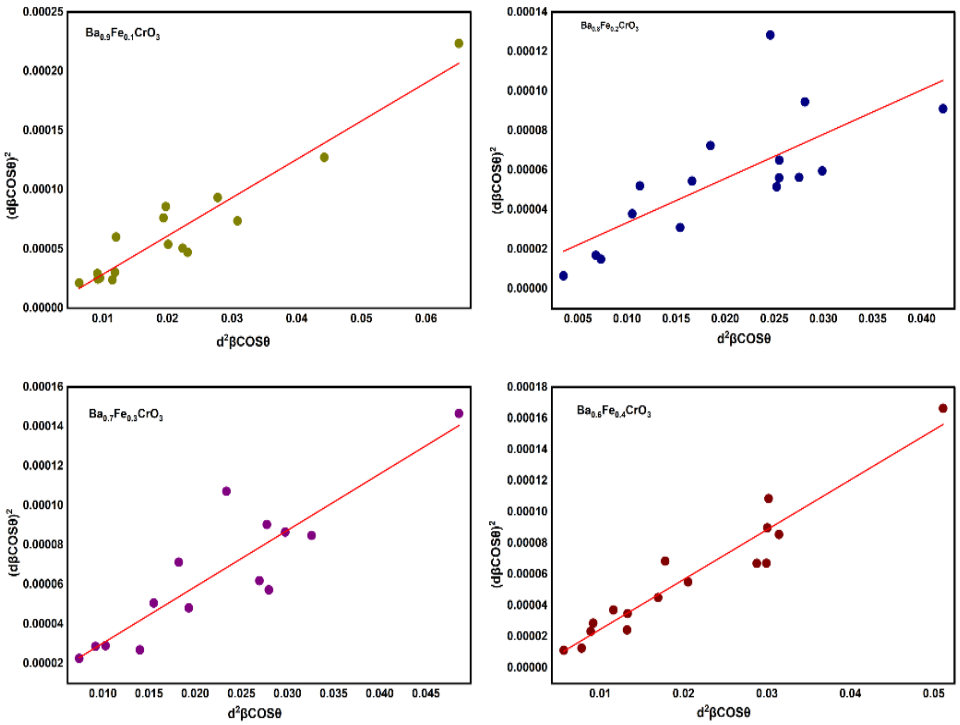

Fig. 6 Size–strain plots of $Ba_{1-x}Fe_xCrO_3$ (BFC1–BFC4) ceramics obtained using the size–strain plot (SSP) method.

Table 4: XRD-derived coherent crystallite/domain size and microstrain parameters of $Ba_{1-x}Fe_xCrO_3$ (BFC-1–BFC-4) obtained using different line-broadening models.

Methods / Materials	DS	WH		HW		MS		SSP		Average
	D_{DS} (nm)	Intercept	D_{WH} (nm)	Slope	D_{HW} (nm)	Intercept	D_{MS} (nm)	Slope	D_{SSP} (nm)	(nm)
BFC1	50.52	0.002	72.41	0.00299	33.45	-5.98285	57.43	0.00324	44.70	51.70
BFC2	56.69	0.00185	78.28	0.00318	31.45	-6.0184	59.51	0.00224	64.65	58.11
BFC3	51.68	0.00204	70.99	0.00291	34.36	-5.98291	57.43	0.00286	50.64	53.02
BFC4	56.35	0.00277	52.28	0.00248	40.32	-5.91761	53.80	0.0032	45.26	49.60

The crystallite-size estimates obtained using the Debye–Scherrer (DS), Williamson–Hall (W–H), Halder–Wagner (H–W), modified Scherrer (M–S), and SSP methods are compared in Table 4. The methods yield different numerical values because they employ different mathematical formulations and assumptions for treating diffraction-line broadening. The arithmetic means of the five estimates are 51.70, 58.11, 53.02, and 49.60 nm for BFC-1 to BFC-4, respectively. These averages provide a convenient summary of the model-derived estimates, with BFC-2 exhibiting the highest mean and BFC-4 the lowest. However, the averages are descriptive summaries, not independent measurements or statistically validated estimates, and do not eliminate the model dependence of the individual methods.

All reported crystallite sizes represent XRD-derived coherent diffraction-domain dimensions rather than physical grain or particle sizes. Furthermore, because an independent

instrumental-broadening profile was unavailable, the results may include contributions from instrumental broadening. Accordingly, the individual estimates and their averages are interpreted as comparative indicators of composition-dependent microstructural variation rather than absolute crystallite sizes.

3.8 Comparative Crystal size

The crystallite sizes estimated using the Debye–Scherrer (DS), Williamson–Hall (WH), Halder–Wagner (HW), modified Scherrer (MS), and size–strain plot (SSP) approaches exhibit appreciable method-dependent variation across the BFC compositions (Fig. 7). For BFC1, the estimated crystallite sizes were 50.52, 72.41, 33.45, 57.43, and 44.70 nm, respectively, while BFC2 exhibited values of 56.69, 78.28, 31.45, 59.51, and 64.65 nm. For BFC3, the corresponding values were 51.68, 70.99, 34.36, 57.43, and 50.64 nm, whereas BFC4 yielded 56.35, 52.28, 40.32, 53.80, and 45.26 nm. Overall, the WH method generally produced relatively larger crystallite-size estimates, whereas the HW method yielded comparatively smaller values for BFC1–BFC3.

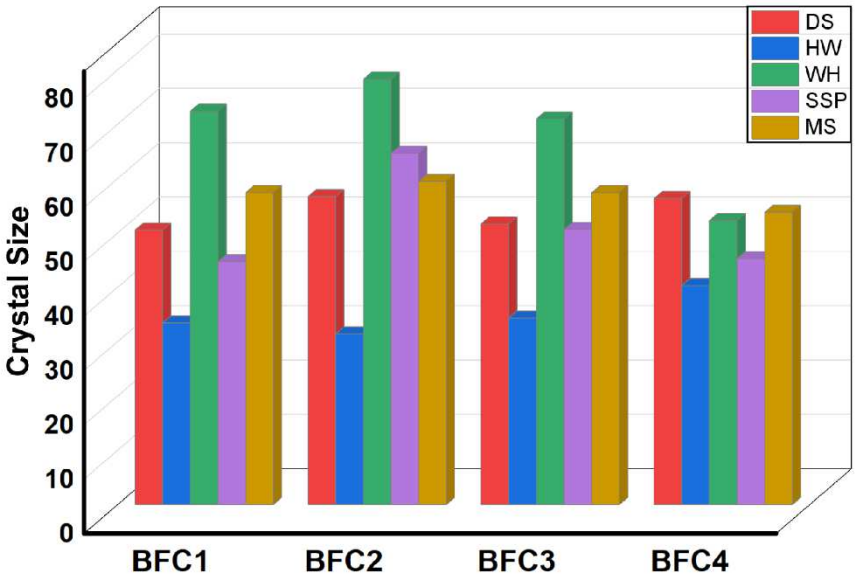

Fig. 7: Comparison of the crystallite sizes of $Ba_{1-x}Fe_xCrO_3$ ceramics determined using different XRD line-broadening methods.

This variation arises from the different mathematical treatments of diffraction-line broadening and the separation of size- and strain-related contributions inherent to each approach. The DS method assumes that the observed peak broadening is predominantly associated with finite crystallite size, whereas WH, HW, and SSP incorporate lattice-strain

effects to different extents. The comparatively close values obtained from multiple approaches nevertheless confirm that the synthesized BFC ceramics possess crystallite dimensions in the nanometer range. The method-dependent variation further highlights the importance of considering both crystallite-size and microstrain contributions when interpreting XRD line broadening [33,34].

3.9 Stacking Faults

The stacking-fault parameter was estimated from the experimentally measured XRD peak characteristics using the relation

$$S_F = \frac{2\pi^2\beta}{45\sqrt{3}\tan\theta} \qquad (4)$$

here β is the fourier coefficient component representing the peak broadening specifically caused by stacking faults and θ is the Bragg angle. The calculated values for BFC-1, BFC-2, BFC-3, and BFC-4 were approximately 0.00142, 0.00132, 0.00141, and 0.00129, respectively (Fig. 8). These values are treated as model-derived indicators of stacking-related planar disorder rather than direct measurements of stacking-fault concentration. The parameter decreases from BFC-1 to BFC-2, increases slightly for BFC-3, and decreases again for BFC-4, indicating a non-monotonic composition dependence. The relatively small variation suggests that the calculated indicator of stacking-related disorder changes modestly across the investigated Fe compositions.

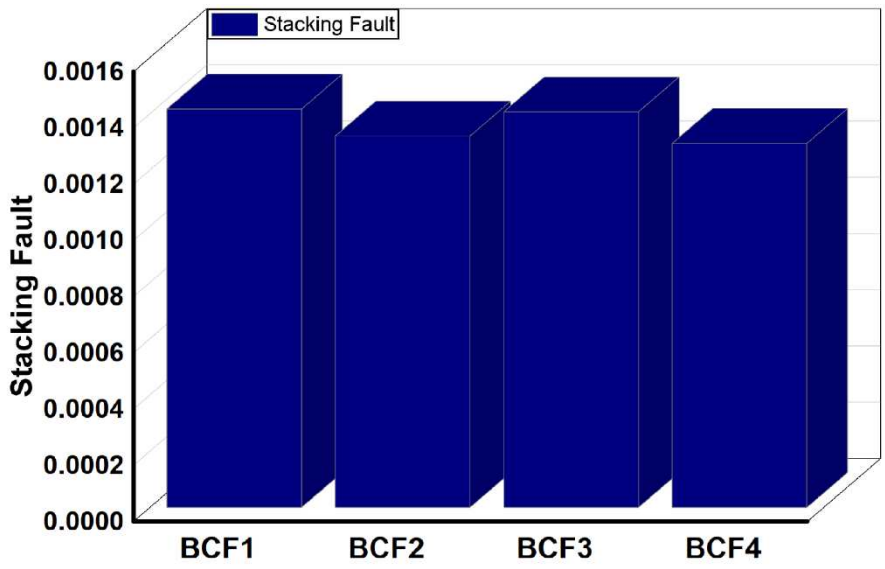

Fig. 8: Variation of the stacking-fault parameter for the BFC1–BFC4 compositions.

However, the estimated parameter depends on the selected reflections, experimental peak-profile determination, instrumental contributions, and the assumptions of the adopted analytical model. Furthermore, the reflection-selection criteria must be appropriate for the structural symmetry of the investigated orthorhombic perovskites; reflection rules developed specifically for HCP crystals cannot be transferred without justification. Accordingly, the results are interpreted comparatively and do not, by themselves, establish a quantitative change in the absolute concentration of stacking faults [35].

3.10 Lattice Strain

Lattice microstrain is associated with local variations in interplanar spacing arising from crystal imperfections, dislocations, and other forms of structural disorder. Such variations can contribute to the broadening of X-ray diffraction (XRD) peaks. In the present study, the Stokes–Wilson (SW) equation was used to estimate the lattice microstrain from the XRD peak-broadening data [36].

$$\xi_{SW} = \beta/4tan\theta \qquad (5)$$

where ξ_{SW} is the Stokes–Wilson microstrain estimate, β is the full width at half maximum (FWHM) of the diffraction peak expressed in radians, and θ is the corresponding Bragg angle. The estimated microstrain values for BFC-1, BFC-2, BFC-3, and BFC-4 were approximately 0.00247, 0.00231, 0.00253, and 0.00233, respectively.

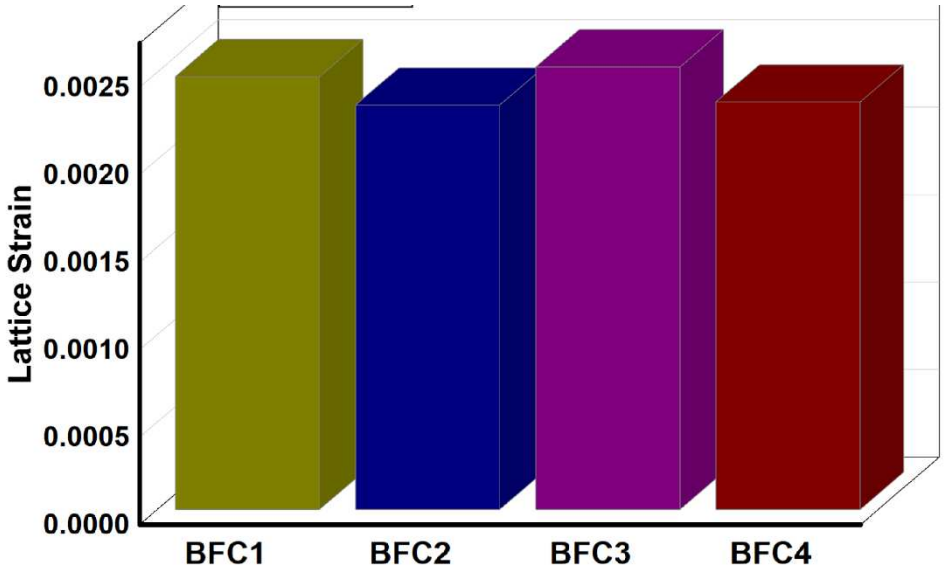

Fig.9: Variation of lattice strain for the BFC1–BFC4 compositions

The calculated values exhibit a non-monotonic composition dependence. The estimated microstrain decreases from BFC-1 to BFC-2, increases for BFC-3, and decreases again for BFC-4. These variations suggest that the XRD-derived microstrain changes with Fe content,

although the trend does not indicate a continuous increase or decrease across the investigated composition range.

It is important to note that the Stokes–Wilson values represent model-dependent estimates derived from diffraction-peak broadening rather than direct measurements of lattice strain. They should also be distinguished from the strain estimates obtained using the Williamson–Hall, Halder–Wagner, and SSP approaches, which employ different analytical treatments of peak broadening. Differences among these models reflect their underlying assumptions and sensitivities; therefore, the SW estimates are interpreted comparatively rather than as definitive absolute values of lattice strain.

Table 5: Stacking-fault probability and lattice strain parameters of $Ba_{1-x}Fe_xCrO_3$ ceramics determined from X-ray diffraction analysis.

Materials	Stacking faults	Lattice Strain
BFC1	1.42×10^{-3}	2.47×10^{-3}
BFC2	1.32×10^{-3}	2.31×10^{-3}
BFC3	1.41×10^{-3}	2.53×10^{-3}
BFC4	1.23×10^{-3}	2.33×10^{-3}

3.11 Dislocation Density

The dislocation-density parameter was estimated from the coherent crystallite size obtained using the DS, W–H, H–W, M–S, and SSP line-broadening approaches. The commonly adopted XRD-based relation was used,

$$\delta = \frac{1}{D^2} \qquad (6)$$

where δ is the dislocation-density parameter ($n\mathrm{m}^{-2}$) and D is the coherent crystallite size expressed in nanometers [37]. Because the different line-broadening methods use different mathematical treatments and assumptions to separate crystallite-size and strain contributions to diffraction broadening, the corresponding D and δ values are not expected to be identical.

The calculated dislocation-density values should therefore be interpreted as model-dependent indicators derived from XRD coherent-domain sizes, not as direct measurements of dislocations. Because the FWHM values were not corrected using an independently measured instrumental-broadening profile, the derived parameters may also be affected by instrumental

contributions to peak broadening. Direct observation of dislocation structures would require complementary characterization, such as transmission electron microscopy. Accordingly, the present results are used for comparative assessment of the microstructural estimates rather than as definitive measurements of absolute dislocation density [38].

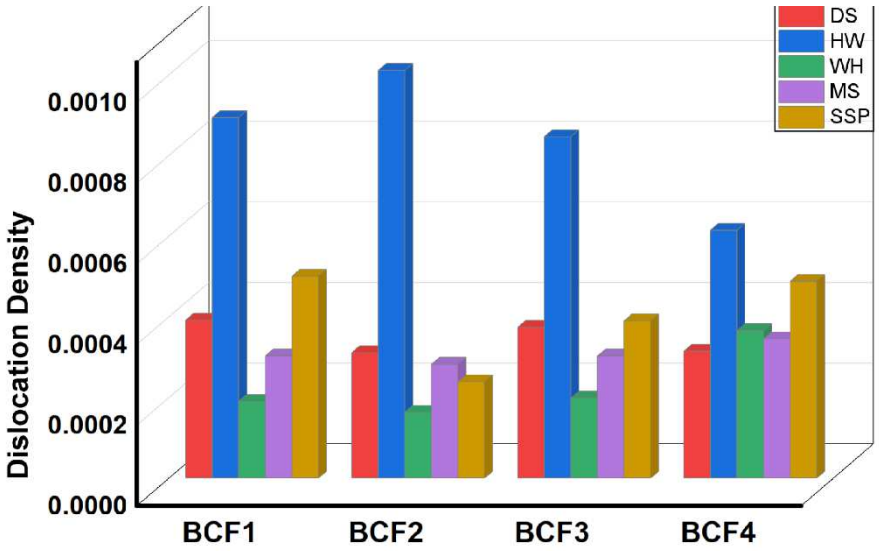

Fig. 10: Several methods used to calculate dislocation densities in BCF samples

Table 6: Comparison of microstructural parameters of $Ba_{1-x}Fe_xCrO_3$ (BFC1–BFC4) ceramics estimated using different strain analysis methods: Debye–Scherrer (DS), Williamson–Hall (WH), Halder–Wagner (HW), Modified Scherrer (MS), and Size–Strain Plot (SSP).

Density / **Materials**	**DS** (nm^{-2})	**WH** (nm^{-2})	**HW** (nm^{-2})	**MS** (nm^{-2})	**SSP** (nm^{-2})
BFC1	3.918×10^{-4}	1.907×10^{-4}	8.940×10^{-4}	3.032×10^{-4}	5.006×10^{-4}
BFC2	3.111×10^{-4}	1.632×10^{-4}	10.1×10^{-4}	2.824×10^{-4}	2.393×10^{-4}
BFC3	3.744×10^{-4}	1.984×10^{-4}	8.468×10^{-4}	3.032×10^{-4}	3.900×10^{-4}
BFC4	3.149×10^{-4}	3.659×10^{-4}	6.150×10^{-4}	3.455×10^{-4}	4.883×10^{-4}

It should be noted that the sizes estimated by the DS, WH, HW, MS, and SSP methods represent XRD-derived coherent diffraction-domain dimensions and should not be interpreted

directly as particle or grain sizes. The differences among the values obtained from these approaches arise partly from their different assumptions concerning the separation of crystallite-size and microstrain contributions to diffraction-line broadening. Therefore, the absolute values obtained from individual methods should be interpreted with appropriate caution, whereas the composition-dependent trends provide a more useful basis for comparison among the $Ba_{1-x}Fe_xCrO_3$ compositions. Direct determination of grain and particle morphology would require complementary techniques such as SEM or TEM, which were not available within the scope of the present study.

3.12 UV–Visible Absorption Analysis

The UV–Visible absorption spectra of $Ba_{1-x}Fe_xCrO_3$ (BFC-1–BFC-4; x = 0.1–0.4) were recorded over 250–1350 nm to examine the composition-dependent optical response (Fig.11) [39]. The spectra exhibit composition-dependent variations in absorption across the measured wavelength range, indicating that Fe-content variation is associated with changes in the optical response of the investigated perovskites [40]. Within the adopted structural model, these changes may be associated with modifications to the local lattice environment and Cr–O electronic framework, together with possible contributions from substitution- and disorder-related electronic states. However, the absorption spectra alone do not establish the specific origin of individual spectral features.

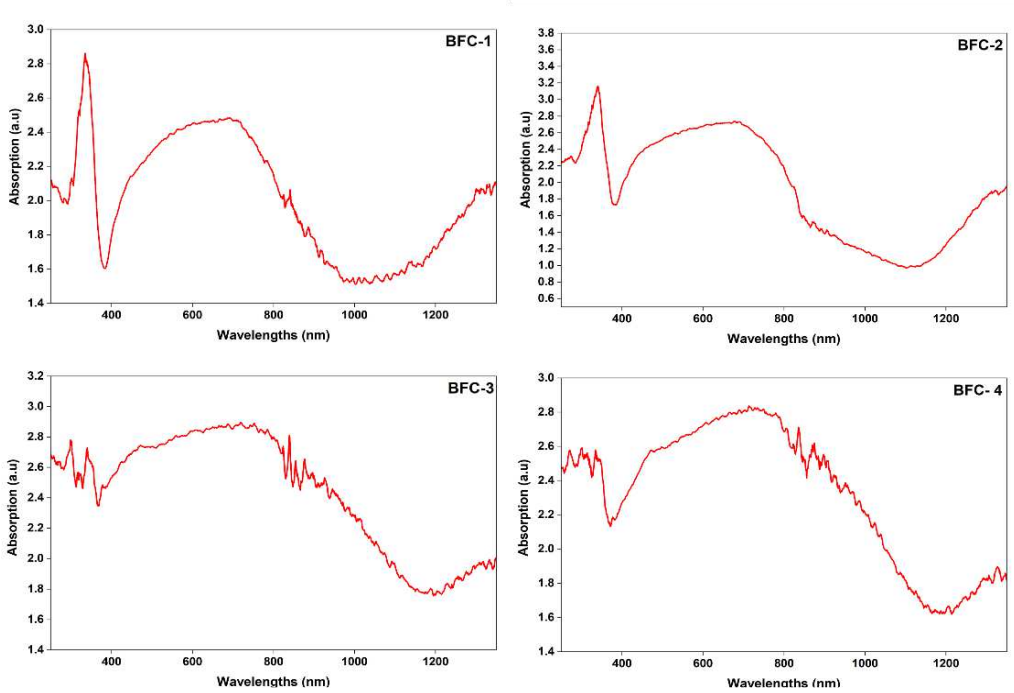

Fig. 11: The UV–Vis absorption profiles of $Ba_{1-x}Fe_xCrO_3$, highlighting Fe-induced modifications in the electronic structure.

BFC-1 (x = 0.1) exhibits a pronounced absorption feature in the 330–360 nm region followed by a marked decrease near 380–400 nm [41,42]. This high-energy absorption can be associated primarily with charge-transfer transitions involving O 2p and Cr 3d states, with possible contributions from Fe-derived states introduced through A-site substitution. A broad

absorption feature extending approximately from 450 to 750 nm is also observed, which may be related to crystal-field-associated d–d transitions of the octahedrally coordinated Cr ions together with defect-related electronic transitions [43]. In the NIR region, the gradual decrease in absorption indicates reduced optical transition probability at lower photon energies.

BFC-1 exhibits distinct spectral variations in the ultraviolet and visible regions, followed by a gradual change in absorption toward the near-infrared (NIR) region. With increasing Fe concentration, BFC-2 shows a modified absorption profile, while BFC-3 and BFC-4 exhibit broader spectral variations and pronounced features in the NIR region. The oscillatory features observed around 800–900 nm, particularly for BFC-3 and BFC-4, may arise from overlapping spectral contributions or measurement-related effects; therefore, they cannot be assigned to specific electronic transitions without further evidence [39–42]. Within the adopted structural model, these composition-dependent changes may reflect the indirect influence of Fe incorporation at the Ba/A-site on the local structure and electronic environment of the perovskite.

Therefore, the spectra indicate that Fe-content variation modifies the optical absorption response of $Ba_{1-x}Fe_xCrO_3$. However, the absorption profiles alone do not establish the origin of individual spectral features or demonstrate a specific optoelectronic application. The optical band-gap trend is therefore evaluated separately using the Tauc analysis.

3.13 Optical Band Gap Analysis

The optical band gap of $Ba_{1-x}Fe_xCrO_3$ (BFC) perovskite samples was estimated using the Tauc relation,

$$(\alpha h\nu)^2 = A(h\nu - E_g) \qquad (7)$$

which corresponds to direct allowed electronic transitions [44]. The band gap energy (E_g) was determined by extrapolating the linear portion of the $(\alpha h\nu)^2$versus photon energy ($h\nu$) plots to the energy axis [45,46]. The estimated band gap values are 3.22, 3.16, 3.01, and 2.99 eV for BFC-1, BFC-2, BFC-3, and BFC-4, respectively (Fig. 12), indicating a progressive red shift of the optical absorption edge with increasing Fe content [47].

The decrease in the Tauc-derived optical band gap may be associated with changes in the local structural and electronic environment accompanying increasing Fe content. Within the adopted structural model, Fe is considered to be incorporated predominantly at the Ba/A-site, indirectly modifying the CrO_6 framework through changes in local electrostatics, lattice geometry, and structural distortion. The comparatively large decrease between BFC-2 and BFC-3 may reflect enhanced structural perturbation or disorder-related contributions, whereas the smaller change between BFC-3 and BFC-4 indicates that the incremental shift in the apparent absorption edge becomes less pronounced at the highest investigated Fe content. These trends do not, however, establish a unique microscopic mechanism.

An additional feature of the Tauc plots is the presence of extended absorption tails toward lower photon energies, including the near-infrared region. Such Urbach-like tails may arise

from localized electronic states associated with structural disorder, microstrain, lattice distortion, and possible defect-related contributions near the band edges. These states may influence the apparent absorption-edge position and contribute to the observed red shift. Nevertheless, the present data do not establish the specific origin of the tails, identify a particular defect species, or demonstrate that oxygen vacancies are responsible.

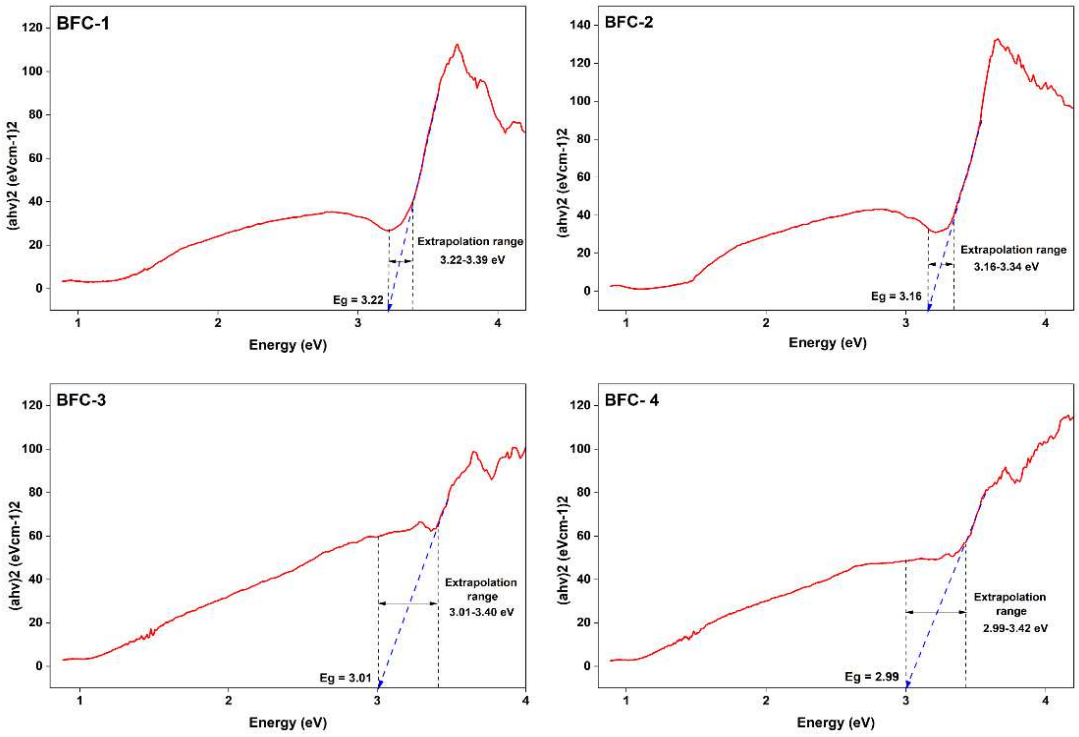

Fig.12: Tauc plots of $Ba_{1-x}Fe_xCrO_3$ perovskites showing the estimation of direct optical band-gap energies

Consequently, the decrease in the Tauc-derived optical band gap should not be interpreted solely as intrinsic band-gap narrowing. Tauc analysis does not independently separate changes in the underlying electronic structure from disorder-related band-tail absorption. A complementary Urbach-energy analysis, based on a suitable linear region of (\ln(\alpha)) versus photon energy, would be needed to quantify the exponential absorption-tail behavior. Because this analysis was not performed in the present study, the reported values are interpreted as Tauc-derived optical band gaps rather than definitive measurements of the fundamental electronic band gaps. Finally, the results demonstrate composition-dependent changes in the optical response, while the relative contributions of intrinsic electronic-structure modification and band-tail absorption remain unresolved.

3.14 Frequency-Dependent Dielectric Constant

The frequency-dependent dielectric constant (ε′) of $Ba_{1-x}Fe_xCrO_3$ (BFC-1–BFC-4) ceramics is presented in Fig. 13. All compositions exhibit a pronounced decrease in ε′ with increasing frequency over the investigated range, followed by a comparatively gradual variation at higher frequencies. This frequency dispersion indicates that the measured dielectric response depends strongly on the timescale of the applied electric field. At lower frequencies,

relatively slow polarization processes, including possible interfacial/space-charge contributions and defect- or dipole-associated polarization, can contribute more effectively to the measured dielectric response. However, the present measurements do not allow these individual contributions to be quantitatively separated [48].

Among the investigated compositions, BFC-3 exhibits the highest low-frequency dielectric constant, reaching approximately 165, followed by BFC-4 (~150), whereas BFC-1 and BFC-2 show substantially lower initial values of approximately 52 and 43, respectively. The enhanced dielectric response of BFC-3 and BFC-4 indicates that Fe incorporation modifies the local structural and polarization environment of the ceramic. However, this enhancement is not strictly proportional to Fe concentration, suggesting that the dielectric response is governed by the combined effects of composition-induced structural distortion, defect-associated polarization, localized charge dynamics, and microstructural characteristics rather than Fe content alone.

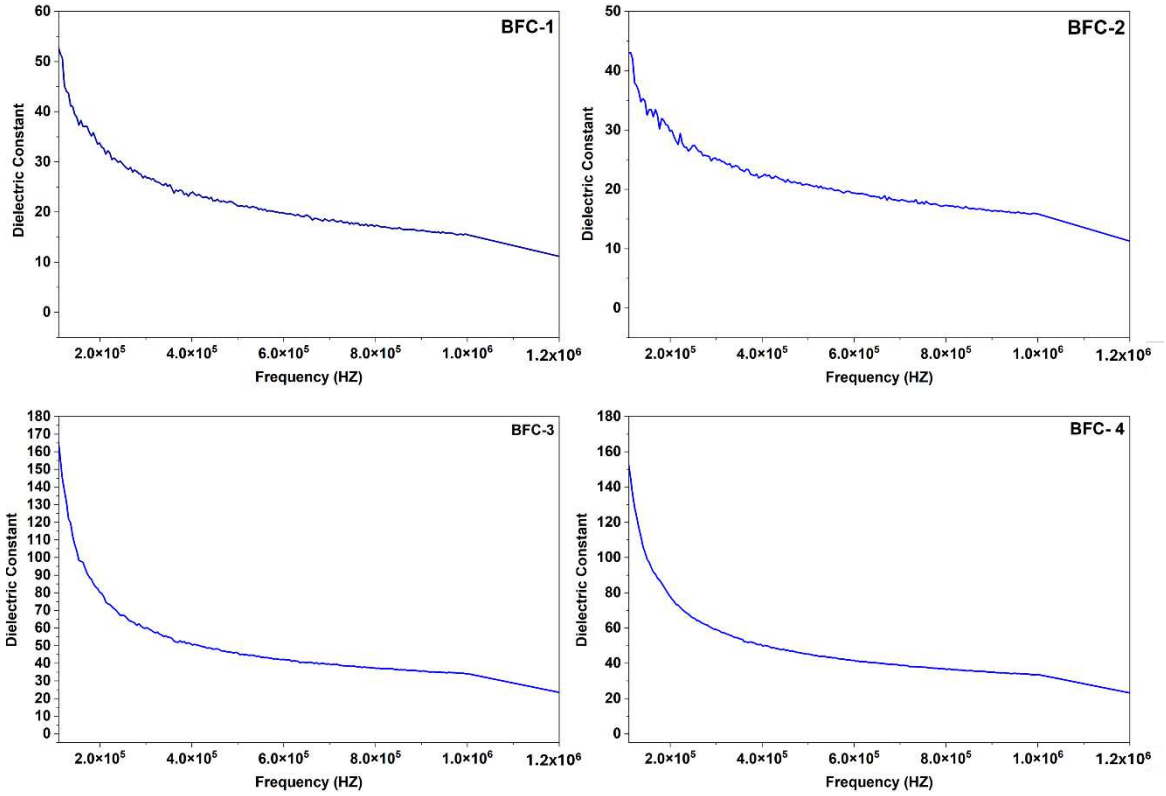

Fig. 13: Frequency-dependent dielectric behavior of $Ba_{1-x}Fe_xCrO_3$ perovskite ceramics

With increasing frequency, ε′ decreases for all compositions because progressively fewer slow polarization species can follow the rapidly alternating electric field. The high-frequency dielectric constants converge toward considerably lower values, approximately 11–23 at the highest measured frequency, indicating the reduced contribution of slow polarization processes. The relatively smooth high-frequency response suggests that the measured dielectric response becomes increasingly dominated by faster polarization processes and the intrinsic lattice response.

The compositional dependence further shows that BFC-3 and BFC-4 retain higher dielectric constants than BFC-1 and BFC-2 across most of the investigated frequency range. This behavior may be associated with changes in the local bonding environment, structural distortion, and defect-associated polarization accompanying Fe incorporation. Nevertheless, the dielectric response is also sensitive to pellet density, grain/grain-boundary characteristics, electrode contact, and measurement conditions. Therefore, the enhanced dielectric constant cannot be attributed exclusively to oxygen-vacancy concentration or any specific defect species without complementary defect-sensitive and impedance-based characterization.

Therefore, the frequency dispersion of ε′ demonstrates that Fe incorporation modifies the polarization characteristics of $Ba_{1-x}Fe_xCrO_3$ ceramics. The relatively high dielectric response of BFC-3 and BFC-4 indicates a composition-dependent modification of the polarization environment, while the pronounced frequency dependence is consistent with contributions from slow and localized polarization processes. However, quantitative separation of interfacial, defect-related, and intrinsic polarization mechanisms would require complementary impedance/Nyquist/Bode analysis, electrical-modulus spectroscopy, and temperature-dependent measurements, which were beyond the scope of the present study.

3.15 Frequency-Dependent Dielectric Loss

The frequency dependence of the dielectric loss (tan δ) of $Ba_{1-x}Fe_xCrO_3$ ceramics (BFC-1–BFC-4) is presented in Fig. 14. All compositions exhibit a pronounced decrease in dielectric loss with increasing frequency, indicating that the dielectric dissipation is strongly frequency dependent.

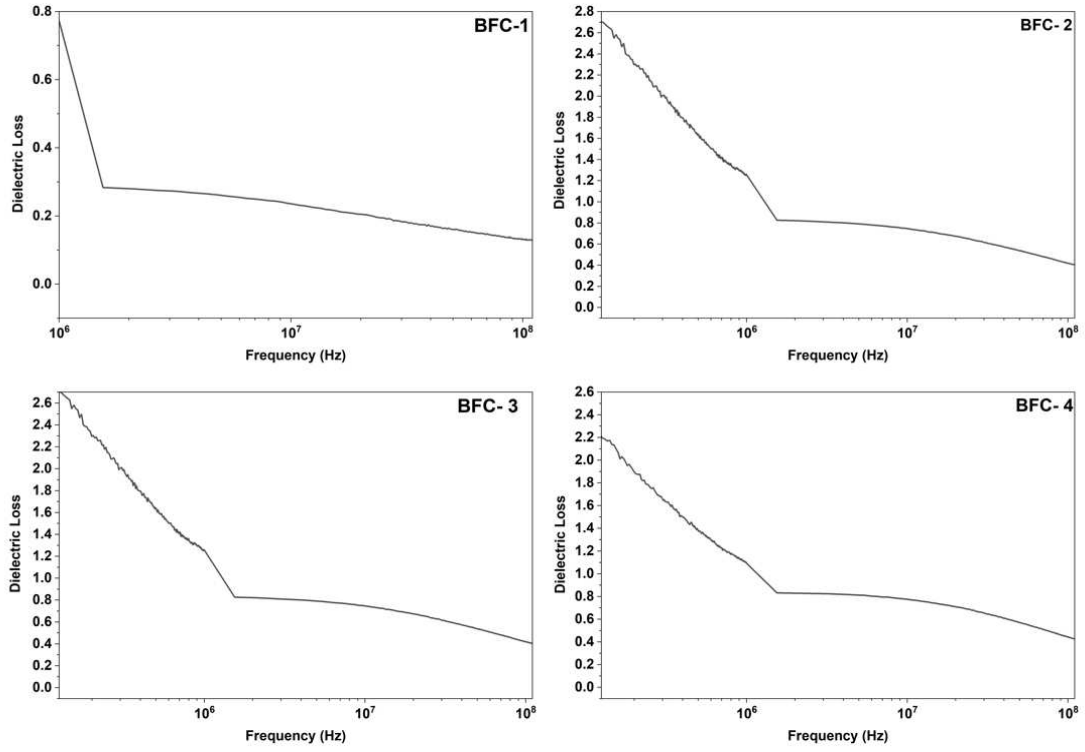

Fig. 14: Variation of dielectric loss (tan δ) with frequency for $Ba_{1-x}Fe_xCrO_3$ perovskites presented using a common logarithmic frequency range of 10^5 – 10^8 Hz.

At lower frequencies, relatively higher tan δ values are observed, which may be associated with contributions from localized charge carriers, slow polarization processes, and interfacial/space-charge effects. As the frequency increases, these slower processes become progressively less able to follow the rapidly alternating electric field, resulting in a reduction in dielectric loss[49].

Among the investigated compositions, BFC-1 exhibits a comparatively low dielectric loss, decreasing from approximately 0.75 at ~10^6 Hz to ~0.13 at 10^8 Hz. In contrast, BFC-2, BFC-3, and BFC-4 show substantially higher losses at the lower end of the measured frequency range, with initial values of approximately 2.7, 2.6, and 2.2, respectively. These samples display a steep decrease up to approximately 10^6–$10^{6.5}$ Hz, followed by a more gradual decline toward ~0.4 at 10^8 Hz. The higher low-frequency loss is consistent with stronger contributions from localized charge dynamics, defect-associated polarization, and interfacial charge accumulation; however, the individual contributions cannot be distinguished quantitatively from the present dielectric-loss measurements alone [50].

No distinct dielectric-loss peak is observed within the investigated frequency range. Therefore, a well-resolved relaxation maximum cannot be identified within the measured window, although a distribution of relaxation times may contribute to the broad low-frequency dispersion. Possible effects of oxygen nonstoichiometry and associated charge-compensation processes cannot be excluded, but they are not directly established by these data. Impedance spectroscopy and electrical-modulus analysis over a range of temperatures would be needed to clarify the underlying relaxation mechanisms.

Overall, the results demonstrate composition- and frequency-dependent dielectric loss in $Ba_{1-x}Fe_xCrO_3$ ceramics, with BFC-1 exhibiting lower loss than the other compositions over the reported range. The observed trends support a cautious correlation between composition, charge dynamics, and dielectric dissipation rather than a definitive assignment of specific microscopic mechanisms.

3.16 Frequency-Dependent AC Conductivity

The frequency-dependent AC conductivity of $Ba_{1-x}Fe_xCrO_3$ ceramics (BFC-1–BFC-4) is presented in Fig. 15. All compositions exhibit a frequency-dependent conductivity response, characterized by relatively weak variation in the lower-frequency region, a pronounced decrease around 1–1.5 MHz, and a subsequent increase toward higher frequencies. The occurrence of this non-monotonic feature at approximately the same frequency for all four compositions suggests that it is a common feature of the measured response; however, its microscopic origin cannot be established from the conductivity data alone [51].

BFC-1 and BFC-2 exhibit comparatively lower AC conductivity, whereas BFC-3 and BFC-4 show substantially higher conductivity over most of the investigated frequency range, particularly at high frequencies. For BFC-1, the conductivity increases gradually from approximately 2.5×10^{-4} S cm^{-1} in the lower-frequency region to approximately 6.5×10^{-4} S cm^{-1} near 1 MHz, before decreasing sharply to approximately 1×10^{-4} S cm^{-1} around 1–1.5 MHz. It subsequently increases with frequency, reaching approximately 2.35×10^{-3} S cm^{-1} at

10^8 Hz. BFC-2 exhibits a similar trend, with conductivity increasing from approximately 2.5 × 10^{-4} S cm^{-1} at low frequencies to approximately 5.8 × 10^{-4} S cm^{-1} near 1 MHz, followed by a sharp decrease and a subsequent increase to approximately 2.65 × 10^{-3} S cm^{-1} at 10^8 Hz.

BFC-3 and BFC-4 display higher conductivity than BFC-1 and BFC-2. For BFC-3, the conductivity remains approximately 2.4 × 10^{-3} S cm^{-1} over much of the lower-frequency region before decreasing to approximately 4 × 10^{-4} S cm^{-1} around 1–1.5 MHz.

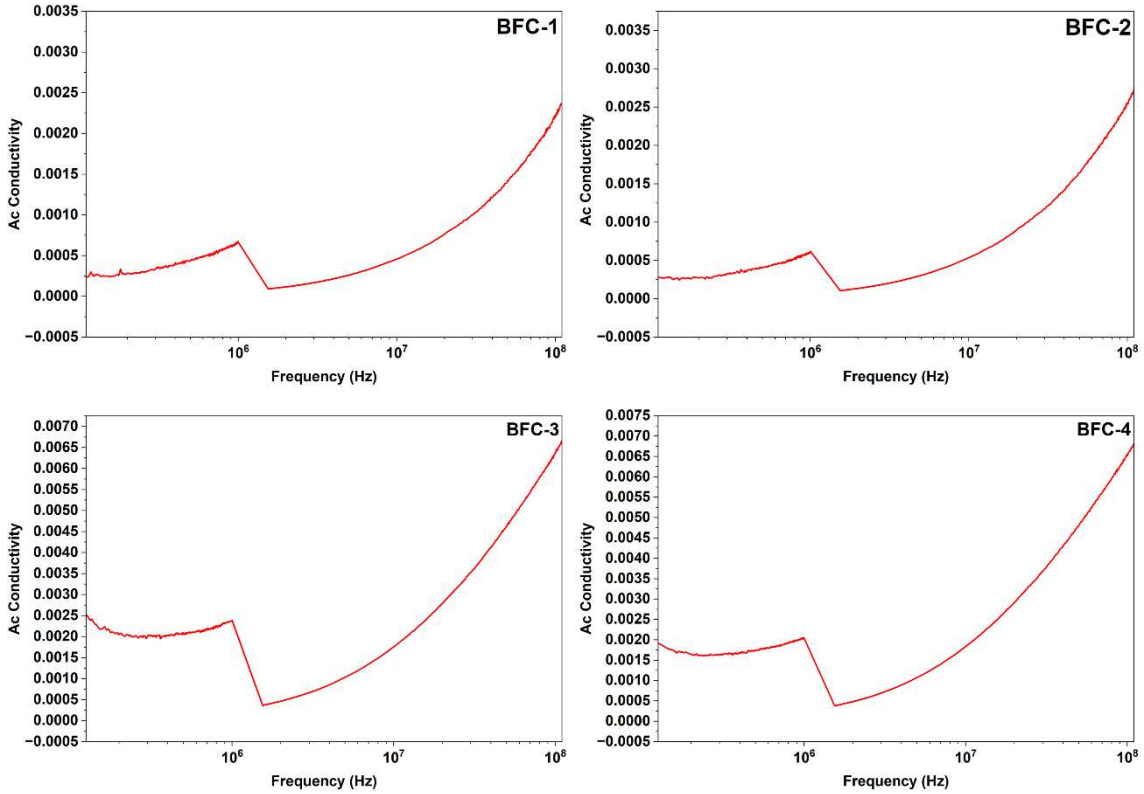

Fig. 15: Frequency-dependent AC conductivity (σ_{AC}) of $Ba_{1-x}Fe_xCrO_3$ ceramics

It then increases progressively, reaching approximately 6.6 × 10^{-3} S cm^{-1} at 10^8 Hz. BFC-4 shows a comparable response, with conductivity decreasing from approximately 2.0 × 10^{-3} S cm^{-1} near 1 MHz to approximately 4 × 10^{-4} S cm^{-1} around 1–1.5 MHz, followed by an increase to approximately 6.8 × 10^{-3} S cm^{-1} at 10^8 Hz. These results indicate that the composition-dependent electrical response is more pronounced for BFC-3 and BFC-4, particularly in the high-frequency region.

The high-frequency increase may be qualitatively associated with localized charge dynamics and frequency-dependent transport in structurally heterogeneous ceramics. However, the intermediate-frequency decrease followed by an increase does not establish a specific hopping process or transition. Contributions from localized transport, defect-associated charge dynamics, electrode/interface effects, or measurement-related factors cannot be distinguished conclusively from the present data.

The frequency-dependent AC conductivity is commonly described phenomenologically by Jonscher's universal power law:

$$\sigma_{AC}(\omega) = \sigma_{DC} + A\omega^{s} \qquad (8)$$

where $\sigma_{AC}(\omega)$ is the AC conductivity, σ_{DC} is the frequency-independent DC conductivity contribution, A is a material and temperature dependent pre-exponential factor, ω is the angular frequency, and s is the frequency exponent. In the present study, the experimental data were not quantitatively fitted to this equation; consequently, σ_{DC}, A, and s were not independently determined. Jonscher's relation is therefore included as a phenomenological framework rather than as a quantitatively validated description of the measured conductivity spectra. Accordingly, the high-frequency conductivity increase should not be regarded as conclusive evidence of a specific Jonscher-type hopping mechanism.

Within the adopted structural model, the higher high-frequency conductivity of BFC-3 and BFC-4 may be associated with composition-induced changes in the local structural environment and localized charge states. Nevertheless, specific mechanisms involving mixed-valence charge compensation, oxygen vacancies, or particular hopping pathways cannot be established without independent characterization of the relevant oxidation states and oxygen content.

So, the measurements demonstrate composition- and frequency-dependent AC conductivity, with BFC-3 and BFC-4 exhibiting higher high-frequency conductivity than BFC-1 and BFC-2. These findings establish a correlation between composition and electrical response but do not independently identify the underlying transport mechanism. Quantitative conductivity fitting, impedance analysis, and temperature-dependent measurements would be needed to clarify the conduction processes.

3.17 FTIR Analysis

Fourier-transform infrared (FTIR) spectroscopy was employed to investigate the local bonding environment and vibrational characteristics of the $Ba_{1-x}Fe_xCrO_3$ ceramics (BFC-1–BFC-4) over the wavenumber range of 4000–500 cm^{-1}, as shown in Fig. 16. The spectra exhibit broadly comparable profiles across the investigated compositions, indicating that Fe incorporation at the Ba-site does not fundamentally alter the parent perovskite-type bonding framework [52]. The principal structural information is obtained from the low-wavenumber region, where vibrations associated with the metal–oxygen framework of the perovskite lattice are expected [53].

A prominent absorption feature near 542 cm^{-1} is observed and can be assigned primarily to vibrations of the Cr–O framework, including stretching/bending modes associated with the CrO_6 octahedra. Because Fe substitutes for Ba at the A-site, its incorporation does not directly replace Cr within the B-site octahedral network. Instead, A-site substitution modifies the local electrostatic environment, lattice dimensions, and bonding geometry surrounding the CrO_6 octahedra. Consequently, changes in the position, intensity, or profile of the low-wavenumber band with Fe content can arise from variations in Cr–O bond lengths, bond angles, octahedral distortion, and defect compensation associated with Fe incorporation.

The persistence of the characteristic low-frequency metal–oxygen vibration throughout the BFC series indicates that the fundamental metal–oxygen framework is retained despite

progressive Fe incorporation. This observation is consistent with the XRD results showing preservation of the orthorhombic perovskite structure over the investigated composition range. Importantly, the FTIR response therefore suggests that Fe acts primarily as an A-site structural modifier, perturbing the local Cr–O environment without generating a distinctly new dominant vibrational framework.

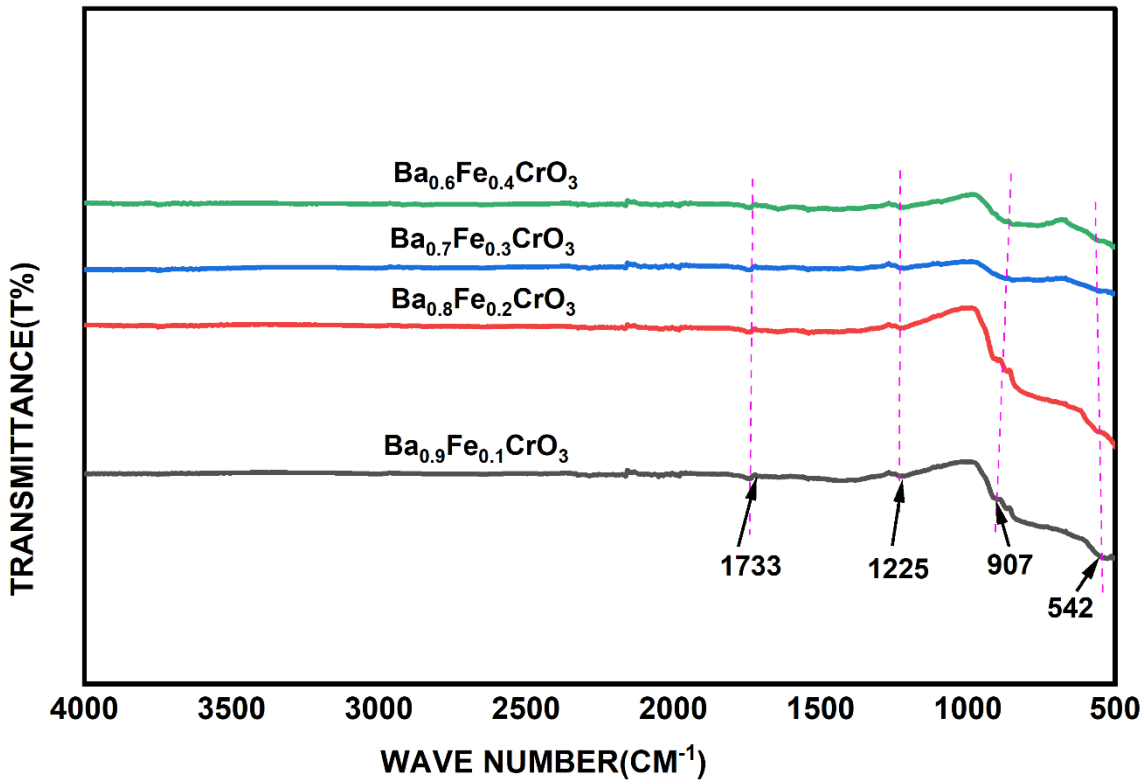

Fig. 16: The FTIR analysis of $Ba_{1-x}Fe_xCrO_3$ (x = 0.1–0.4) ceramics illustrating the evolution of metal–oxygen vibrational modes

Additional weak features are observed near 907, 1225, and 1733 cm^{-1}. These bands are considerably less characteristic of the fundamental metal–oxygen lattice vibrations and may be associated with surface-adsorbed species, residual molecular groups, or carbon-containing surface species introduced during processing or subsequent sample handling. The feature near 1733 cm^{-1}, in particular, may be related to C=O-containing surface species, whereas bands in the intermediate-wavenumber region can arise from weak surface-related vibrational contributions. Because these features are relatively weak and no strong broad O–H stretching band is evident in the 3200–3600 cm^{-1} region, such contributions are unlikely to represent the dominant bonding structure of the ceramic [52–55].

The FTIR spectra do not provide compelling evidence for a substantial amount of residual precursor or secondary carbonate species. Nevertheless, FTIR alone cannot establish phase purity, and the absence of secondary phases should primarily be established from XRD phase identification and refinement. The dominant low-wavenumber metal–oxygen vibration,

together with the XRD results, supports the successful development of the perovskite oxide framework.

With increasing Fe content, the broadly preserved spectral profile indicates that A-site Fe incorporation occurs within the existing perovskite framework rather than producing a fundamentally different bonding structure. Nevertheless, subtle variations in the intensity and shape of the low-frequency vibrational band can be associated with A-site chemical substitution, local lattice distortion, and charge-compensation-related defects. In particular, replacing Ba^{2+} with Fe of a different oxidation state can perturb local charge neutrality and may promote changes in Cr oxidation state and/or oxygen-vacancy concentration. These effects can indirectly modify the Cr–O bonding environment and octahedral distortion.

Therefore, the FTIR results confirm the persistence of the characteristic metal–oxygen framework of $Ba_{1-x}Fe_xCrO_3$ and demonstrate that Fe incorporation at the Ba A-site primarily modifies the local structural environment surrounding the CrO_6 octahedra rather than directly replacing the Cr-site cations.

3.18 Comparative Analysis

A comparative overview of the previously reported $BaFeO_3$-based system [56] and the present $Ba_{1-x}Fe_xCrO_3$ perovskites is presented in Table 7.

Table 7: Comparative overview of the structural, optical, dielectric, and electrical properties of the previously reported $BaFeO_3$-based system and the present $Ba_{1-x}Fe_xCrO_3$ perovskites.

Property	**Previous $BaFeO_3$-based study**	**Present $Ba_{1-x}Fe_xCrO_3$ study**
Nominal composition	$BaFeO_3$-based perovskites with Cr-site engineering	$Ba_{1-x}Fe_xCrO_3$, x = 0.1–0.4
Structural identification	Orthorhombic, based on XRD phase identification	Orthorhombic, based on XRD phase identification
Lattice-parameter variation	Nonlinear variation with Cr concentration	Non-monotonic variation with Fe concentration
Reported lattice-parameter ranges	a = 7.009–11.7051 Å; b = 5.7577–8.1632 Å; c = 4.2031–6.7531 Å	a = 9.6312–16.4494 Å; b = 7.0841–9.7133 Å; c = 4.7531–7.1219 Å
Reported unit-cell-volume range	188.61–450.00 Å³	476.53–785.19 Å³
XRD-derived coherent-domain size	Approximately 22.17–102.71 nm across five line-broadening models	Approximately 31–78 nm across five line-broadening models

Tauc-derived optical band gap	2.948–3.238 eV	2.99–3.22 eV
Main research emphasis	Relationships among Cr-site engineering, structural defects, electronic structure, optical response, and charge transport	Relationships among Fe content, XRD-derived microstructural characteristics, optical response, dielectric properties, and AC conductivity
Principal interpretive limitation	Quantitative comparison depends on the crystallographic and analytical methods reported in the original study	Cation-site occupancy and oxidation states are not directly established; crystallographic parameters and line-broadening estimates require cautious interpretation

4. Limitations and Scope of Structural Interpretation

The structural and defect-related interpretations in this study should be considered in the context of the available characterization techniques. XRD and FTIR provide complementary information on the perovskite structure and metal–oxygen lattice vibrations, but they do not independently establish cation-site occupancy, oxidation states, or oxygen nonstoichiometry. Accordingly, predominant Fe incorporation at the Ba/A-site is treated as a working structural model rather than a definitive site-occupancy determination; partial Fe occupancy at the Cr/B-site cannot be excluded.

Possible oxygen nonstoichiometry and associated charge-compensation processes are discussed as potential contributors to the observed structural, optical, dielectric, and electrical responses, but they are not directly established by the present measurements. Further investigation using XPS, XANES/EXAFS, Mössbauer spectroscopy, quantitative oxygen-content analysis, and appropriate structural refinement would help clarify cation valence, site occupancy, and oxygen stoichiometry. In addition, SEM/TEM characterization would provide complementary information on grain morphology, aggregation, and microstructural defects. These investigations are important directions for future work and would help distinguish the proposed mechanisms from the experimentally established composition-dependent trends.

5. Conclusions

This study investigated the composition-dependent structural, microstructural, optical, dielectric, and AC-conductivity properties of $Ba_{1-x}Fe_xCrO_3$ ceramics (x = 0.1–0.4). XRD indicated an orthorhombic perovskite framework without detectable secondary crystalline phases within the measurement limits. The indexed lattice parameters and XRD-derived microstructural parameters varied with composition, while five line-broadening methods yielded different coherent-domain size estimates, highlighting their model dependence.

The Tauc-derived optical band gap decreased from 3.22 to 2.99 eV with increasing Fe content, indicating a composition-dependent shift in the optical absorption edge. Dielectric and AC-conductivity measurements also revealed composition- and frequency-dependent responses. BFC-3 and BFC-4 exhibited higher high-frequency conductivity, whereas BFC-1 showed comparatively lower dielectric loss, demonstrating trade-offs rather than uniform improvement across all functional properties. The conductivity decrease around 1–1.5 MHz remains unexplained, and quantitative Jonscher-law parameters were not determined.

Within the adopted structural model, Fe is considered predominantly associated with the Ba/A-site; however, partial B-site incorporation cannot be excluded because direct site-occupancy characterization was not performed. Similarly, oxygen nonstoichiometry and associated charge-compensation mechanisms remain possible but unverified explanations for the observed property variations. Overall, the results establish composition-dependent correlations among structural, optical, dielectric, and electrical characteristics without conclusively identifying the underlying defect or transport mechanisms. Further studies involving direct site-occupancy and chemical-state analysis, oxygen-content measurements, impedance spectroscopy, temperature-dependent electrical characterization, and complementary microstructural techniques are needed to clarify these mechanisms and assess potential functional-oxide applications.

Acknowledgments

The authors gratefully acknowledge Institute of Nuclear Science & Technology, Bangladesh Atomic Energy Commission, and Bangladesh Council of Scientific & Industrial Research (BCSIR), Dhaka Laboratories, Bangladesh for providing the necessary experimental facilities to carry out this research. The authors also extend their sincere appreciation to CRIR, National Institute of Textile Engineering and Research for the valuable cooperation and continuous support throughout the study, and to the International Atomic Energy Agency (IAEA) for providing financial support in the Research Contract No. 29378, Coordinated Research Project F12027 for the chemicals and research.

Declarations

Clinical Trial Registration

Not applicable. This study does not involve human participants or clinical trials.

Ethics, Consent to Participate, and Consent to Publish declarations

Ethics, Consent to Participate, and Consent to Publish declarations: not applicable.

Declaration of generative AI and AI-assisted technologies

During the preparation of this manuscript, the authors used ChatGPT to improve language and readability. After using this tool, the authors reviewed and edited the content as needed and take full responsibility for the final manuscript.

Availability of Data

The data supporting the findings of this study are available within the article. Additional data related to this study are available from the corresponding author upon reasonable request.

Disclosure statement

No potential conflict of interest was reported by the author(s).

Funding

The authors declare that no funds, grants, or other financial support were received during the research work or preparation of this manuscript.

Authors' contributions

A. Alam, and S. Hossain contributed to the research planning, material synthesis, data acquisition, data analysis, data interpretation, and manuscript writing. M. S. Akter, and S. Akter contributed to the material synthesis, data acquisition and data interpretation. M. R. Hasan and M. A. Rob contributed to data analysis, data interpretation, and manuscript review-editing. J. Maudood, M. S. Islam, N. Khatun, S. Islam, and A. K. Azad all have given support in data acquisition and interpretation. S. Hossain and M. S. Alam have supervised the research work.

Reference

[1] C. Sun, J.A. Alonso, J. Bian, Recent Advances in Perovskite-Type Oxides for Energy Conversion and Storage Applications, Adv. Energy Mater. 11 (2021) 2000459. https://doi.org/10.1002/AENM.202000459;REQUESTEDJOURNAL:JOURNAL:16146840;WGROUP:STRING:PUBLICATION.

[2] J. Zhu, H. Li, L. Zhong, P. Xiao, X. Xu, X. Yang, Z. Zhao, J. Li, Perovskite oxides: preparation, characterizations, and applications in heterogeneous catalysis, ACS Publications 4 (2014) 2917–2940. https://doi.org/10.1021/CS500606G.

[3] K. Wang, C. Han, Z. Shao, J. Qiu, S. Wang, S. Liu, Perovskite oxide catalysts for advanced oxidation reactions, Wiley Online Library 31 (2021). https://doi.org/10.1002/ADFM.202102089.

[4] T. Liu, S. Ma, X. Zhang, J. Wang, Z. Tian, Y. Dou, Z. Peng, T. Ouyang, B. Lin, X. He, W. Tao, Y. Niu, Y. Niu, Synergistic Electronic Descriptors for $BaMO_3$ (M=Sc to Zn) Perovskite ORR/OER Electrocatalysis: Decoding Bond Strength, Orbital Hybridization, and Electron Transfer Synergy, (2025). https://doi.org/10.2139/SSRN.5589106.

[5] A.B.J. Kharrat, From crystal chemistry to optical functionality in rare-earth orthochromites: a unified physical framework, Journal of the Iranian Chemical Society 2026 23:6 23 (2026) 138-. https://doi.org/10.1007/S13738-026-03442-W.

[6] R.M. Wood, K.A. Abboud, R.C. Palenik, G.J. Palenik, Bond valence sums in coordination chemistry. Calculation of the oxidation state of chromium in complexes containing only Cr-O bonds and a redeterminafion of the crystal structure of potassium Tetra(peroxo)ehromate(V), Inorg. Chem. 39 (2000) 2065–2068. https://doi.org/10.1021/IC990982C/SUPPL_FILE/IC990982C.CIF.

[7] N. Pathak, P.S. Ghosh, S.K. Gupta, R.M. Kadam, A. Arya, Defects induced changes in the electronic structures of MgO and their correlation with the optical properties: a special case of electron–hole recombination from the conduction band, RSC Adv. 6 (2016) 96398–96415. https://doi.org/10.1039/C6RA21065A.

[8] C. Feng, M.B. Faheem, J. Fu, Y. Xiao, C. Li, Y. Li, Fe-Based Electrocatalysts for Oxygen Evolution Reaction: Progress and Perspectives, ACS Catal. 10 (2020) 4019–4047. https://doi.org/10.1021/ACSCATAL.9B05445.

[9] D. Friebel, M.W. Louie, M. Bajdich, K.E. Sanwald, Y. Cai, A.M. Wise, M.J. Cheng, D. Sokaras, T.C. Weng, R. Alonso-Mori, R.C. Davis, J.R. Bargar, J.K. Nørskov, A. Nilsson, A.T. Bell, Identification of Highly Active Fe Sites in (Ni,Fe)OOH for Electrocatalytic Water Splitting, J. Am. Chem. Soc. 137 (2015) 1305–1313. https://doi.org/10.1021/JA511559D.

[10] A. Kumar, M.K. Warshi, A. Sagdeo, P.R. Sagdeo, Investigations on the Electronic Structure of the Strongly Correlated Electron System Cr-Doped PrFeO3, The Journal of Physical Chemistry C 125 (2021) 14048–14055. https://doi.org/10.1021/ACS.JPCC.1C02719.

[11] P. Karki, R. Bhimireddi, L. Dhavala, A. V. Anupama, A.M. Rao, R. Karreddula, A.A. Ansari, Structural, Optical, and Magnetic Properties of Brownmillerite KBiFe2O5 and KBiFe1.95Ti0.05O5+ via Reactive Templated Method, ACS Omega 9 (2024) 43948–43955. https://doi.org/10.1021/ACSOMEGA.4C07882.

[12] C. Venkatrao, D.R.S. Reddy, R. Bhimireddi, Optimization of sintering temperature for realizing enhanced magnetic properties of YFeO3 ceramic derived from the sol-gel technique, Journal of Materials Science: Materials in Electronics 33 (2022) 20731–20739. https://doi.org/10.1007/S10854-022-08883-6/METRICS.

[13] Y.S. Madansure, S.K. Gurav, S.D. Balsure, P.K. Gaikwad, A. Imran, A.M. El-Toni, A. V. Fulari, S.E. Shirsath, R.H. Kadam, X-ray diffraction analysis by Williamson-Hall, strain-size, Halder-Wagner, and Nelson–Riley methods, and its co-relationship with elastic and magnetic properties of Ce3+ substituted Fe-rich cobalt ferrite, Journal of Materials Science: Materials in Electronics 2026 37:10 37 (2026) 706-. https://doi.org/10.1007/S10854-026-17126-X.

[14] M.R. Hasan, S. Hossain, M.M. Parvez, J. Maudood, M.S. Islam, A. Alam, S. Islam, N. Khatun, M.A. Rob, F. Ahmed, M.S. Aktar, M.M. Tasnim, Structural and electrical properties of Yb, Sn doped barium zirconate as a novel perovskite, Materials Research Innovations (2025). https://doi.org/10.1080/14328917.2025.2571956.

[15] M. Aykol, J.H. Montoya, J. Hummelshøj, Rational Solid-State Synthesis Routes for Inorganic Materials, J. Am. Chem. Soc. 143 (2021) 9244–9259. https://doi.org/10.1021/JACS.1C04888.

[16] A. Kumar, S. Dutta, S. Kim, T. Kwon, S.S. Patil, N. Kumari, S. Jeevanandham, I.S. Lee, Solid-State Reaction Synthesis of Nanoscale Materials: Strategies and Applications, Chem. Rev. 122 (2022) 12748–12863. https://doi.org/10.1021/ACS.CHEMREV.1C00637.

[17] A. Alam, Md.R. Hasan, Md.A. Rob, Md.R. Islam, Md.S. Islam, A.K. Azad, S. Hossain, Md.S. Alam, Predicting Sintering Temperatures of Perovskite Oxides from Melting Temperature: A Literature-Based Framework, Transactions of the Indian Institute of Metals 2026 79:11 79 (2026) 260-. https://doi.org/10.1007/S12666-026-04016-3.

[18] M. Deng, Z. Lei, X. Li, Y. Li, L. Fu, G. Cai, Reducing sintering temperature and regulating properties via forming crystalline-amorphous dual-phase microstructure, J. Alloys Compd. 1069 (2026) 188626. https://doi.org/10.1016/J.JALLCOM.2026.188626.

[19] S.C. Tidrow, Mapping Comparison of Goldschmidt's Tolerance Factor with Perovskite Structural Conditions, Ferroelectrics 470 (2014) 13–27. https://doi.org/10.1080/00150193.2014.922372.

[20] K.Y. Tsui, N. Onishi, R.F. Berger, Tolerance Factors Revisited: Geometrically Designing the Ideal Environment for Perovskite Dopants, Journal of Physical Chemistry C 120 (2016) 23293–23298. https://doi.org/10.1021/ACS.JPCC.6B09277.

[21] D. Ji, S.Z. Feng, L. Wang, S. Wang, M. Na, H. Zhang, C.M. Zhang, X. Li, Regulatory tolerance and octahedral factors by using vacancy in APbI3 perovskites, Vacuum 164 (2019) 186–193. https://doi.org/10.1016/J.VACUUM.2019.03.018.

[22] T. Sato, S. Takagi, S. Deledda, B.C. Hauback, S.I. Orimo, Extending the applicability of the Goldschmidt tolerance factor to arbitrary ionic compounds, Scientific Reports 2016 6:1 6 (2016) 23592-. https://doi.org/10.1038/srep23592.

[23] Y. Wang, Y. Wang, T.A.S. Doherty, S.D. Stranks, F. Gao, D. Yang, Octahedral units in halide perovskites, Nature Reviews Chemistry 2025 9:4 9 (2025) 261–277. https://doi.org/10.1038/s41570-025-00687-6.

[24] M. Becker, T. Klüner, M. Wark, Formation of hybrid ABX3 perovskite compounds for solar cell application: first-principles calculations of effective ionic radii and determination of tolerance factors, Dalton Transactions 46 (2017) 3500–3509. https://doi.org/10.1039/C6DT04796C.

[25] Rethinking tolerance factor analysis for chalcogenide perovskites - Materials Horizons (RSC Publishing) DOI:10.1039/D4MH00689E, (n.d.). https://pubs.rsc.org/en/content/articlehtml/2024/mh/d4mh00689e (accessed June 24, 2026).

[26] U.Z. Mohamad Zaidi, A.R. Bushroa, R.R. Ghahnavyeh, R. Mahmoodian, Crystallite size and microstrain: XRD line broadening analysis of AgSiN thin films, Pigment & Resin Technology 48 (2019) 473–480. https://doi.org/10.1108/PRT-03-2018-0026.

[27] S.A. Disha, M. Sahadat Hossain, M.L. Habib, S. Ahmed, Calculation of crystallite sizes of pure and metals doped hydroxyapatite engaging Scherrer method, Halder-Wagner method, Williamson-Hall model, and size-strain plot, Results in Materials 21 (2024) 100496. https://doi.org/10.1016/J.RINMA.2023.100496.

[28] M. Kawsar, M.S. Hossain, N.M. Bahadur, S. Ahmed, Synthesis of nano-crystallite hydroxyapatites in different media and a comparative study for estimation of crystallite size using Scherrer method, Halder-Wagner method size-strain plot, and Williamson-Hall model, Heliyon 10 (2024) e25347. https://doi.org/10.1016/j.heliyon.2024.e25347.

[29] A. Monshi, M.R. Foroughi, M.R. Monshi, Modified Scherrer Equation to Estimate More Accurately Nano-Crystallite Size Using XRD, World Journal of Nano Science and Engineering 2 (2012) 154–160. https://doi.org/10.4236/wjnse.2012.23020.

[30] S. Nasiri, M. Rabiei, A. Palevicius, G. Janusas, A. Vilkauskas, V. Nutalapati, A. Monshi, Modified Scherrer equation to calculate crystal size by XRD with high accuracy, examples Fe2O3, TiO2 and V2O5, Nano Trends 3 (2023) 100015. https://doi.org/10.1016/J.NWNANO.2023.100015.

[31] S. Mustapha, M.M. Ndamitso, A.S. Abdulkareem, J.O. Tijani, D.T. Shuaib, A.K. Mohammed, A. Sumaila, Comparative study of crystallite size using Williamson-Hall and Debye-Scherrer plots for ZnO nanoparticles, Advances in Natural Sciences: Nanoscience and Nanotechnology 10 (2019) 045013. https://doi.org/10.1088/2043-6254/AB52F7.

[32] A. Pal, A dimensionally consistent size–strain plot method for crystallite size and microstrain estimation, J. Alloys Compd. 1048 (2025) 185324. https://doi.org/10.1016/J.JALLCOM.2025.185324.

[33] O. V. Merkulov, A.A. Markov, I.A. Leonidov, M. V. Patrakeev, V.L. Kozhevnikov, Oxygen nonstoichiometry and thermodynamic quantities in solid solution SrFe1–xSnxO3–δ, J. Solid State Chem. 262 (2018) 121–126. https://doi.org/10.1016/J.JSSC.2018.03.010.

[34] J.I. Langford, A.J.C. Wilson, Scherrer after sixty years: A survey and some new results in the determination of crystallite size, Urn:Issn:0021-8898 11 (1978) 102–113. https://doi.org/10.1107/S0021889878012844.

[35] M.A. Rob, S. Alam, M.R. Hasan, A. Mahmud, J. Maudood, M.S. Islam, M.M. Rahman, S. Islam, A. Siddika, F. Ahmed, S. Hossain, Structural characterization and functional tailoring of Zr-induced $SrFeO_3$ perovskites synthesized by solid-state sintering route, Journal of Materials Science: Materials in Electronics 2026 37:7 37 (2026) 476-. https://doi.org/10.1007/S10854-026-16873-1.

[36] R. Rai, T. Triloki, B.K. Singh, X-ray diffraction line profile analysis of KBr thin films, Appl. Phys. A Mater. Sci. Process. 122 (2016) 774-. https://doi.org/10.1007/S00339-016-0293-3/METRICS.

[37] A.K. Mondal, L.K. Ping, M.A. Shazni Mohammad Haniff, M.A. Mohd Sarjidan, B.T. Goh, M.A. Mohamed, Temperature Dependence of Ultrathin Mixed-Phase Ga2O3 Films Grown on the α-Al2O3 Substrate via Mist-CVD, ACS Omega 7 (2022) 2252. https://doi.org/10.1021/ACSOMEGA.1C05859.

[38] J. Gubicza, Reliability and interpretation of the microstructural parameters determined by X-ray line profile analysis for nanostructured materials, The European Physical Journal Special Topics 2022 231:24 231 (2022) 4153–4165. https://doi.org/10.1140/EPJS/S11734-022-00572-Z.

[39] M.S.H. Akash, K. Rehman, Ultraviolet-Visible (UV-VIS) Spectroscopy, Essentials of Pharmaceutical Analysis (2020) 29–56. https://doi.org/10.1007/978-981-15-1547-7_3.

[40] R.S. Pavlov, V.B. Marzá, J.B. Carda, Electronic absorption spectroscopy and colour of chromium-doped solids, J. Mater. Chem. 12 (2002) 2825–2832. https://doi.org/10.1039/B201802K.

[41] F.H. ElBatal, M.S. Selim, S.Y. Marzouk, M.A. Azooz, UV-vis absorption of the transition metal-doped SiO2–B2O3–Na2O glasses, Physica B Condens. Matter 398 (2007) 126–134. https://doi.org/10.1016/J.PHYSB.2007.05.004.

[42] T. Linnert, P. Mulvaney, A. Henglein, H. Weller, Long-lived nonmetallic silver clusters in aqueous solution: preparation and photolysis, J. Am. Chem. Soc. 112 (2002) 4657–4664. https://doi.org/10.1021/JA00168A005.

[43] R.A. Schoonheydt, UV-VIS-NIR spectroscopy and microscopy of heterogeneous catalysts, Chem. Soc. Rev. 39 (2010) 5051–5066. https://doi.org/10.1039/C0CS00080A.

[44] D. Dristy, M. Hasan, S. Hossain, M. Parvez, A.A.-N. Materials, undefined 2026, Structural and optical characterization of Ni–Zn and Sn–Zn co-doped CdS nanoparticles synthesized via hydrothermal method, ElsevierDR Dristy, MR Hasan, S Hossain, MM Parvez, A Alam, MR Bhuiyan, F Ahmed, S IslamNext Materials, 2026•Elsevier (n.d.). https://www.sciencedirect.com/science/article/pii/S2949822826013110 (accessed September 8, 2026).

[45] P. Makuła, M. Pacia, W. Macyk, How To Correctly Determine the Band Gap Energy of Modified Semiconductor Photocatalysts Based on UV-Vis Spectra, Journal of Physical Chemistry Letters 9 (2018) 6814–6817. https://doi.org/10.1021/ACS.JPCLETT.8B02892/SUPPL_FILE/JZ8B02892_LIVESLIDES.MP4.

[46] Y. Wang, K. Lopata, S.A. Chambers, N. Govind, P. V. Sushko, Optical Absorption and Band Gap Reduction in (Fe1–xCrx)2O3 Solid Solutions: A First-Principles Study, Journal of Physical Chemistry C 117 (2013) 25504–25512. https://doi.org/10.1021/JP407496W.

[47] J. Klein, L. Kampermann, B. Mockenhaupt, M. Behrens, J. Strunk, G. Bacher, Limitations of the Tauc Plot Method, Adv. Funct. Mater. 33 (2023) 2304523. https://doi.org/10.1002/ADFM.202304523;WEBSITE:WEBSITE:ADVANCED;CTYPE:STRING:JOURNAL.

[48] B. Harihara Venkataraman, K.B.R. Varma, Frequency-dependent dielectric characteristics of ferroelectric SrBi2Nb2O9 ceramics, Solid State Ion. 167 (2004) 197–202. https://doi.org/10.1016/J.SSI.2003.12.020.

[49] A.M. Shaikh, S.S. Bellad, B.K. Chougule, Temperature and frequency-dependent dielectric properties of Zn substituted Li–Mg ferrites, J. Magn. Magn. Mater. 195 (1999) 384–390. https://doi.org/10.1016/S0304-8853(99)00138-9.

[50] P.S. Padhi, S.K. Rai, H. Srivastava, R.S. Ajimsha, A.K. Srivastava, P. Misra, Maxwell–Wagner Relaxation-Driven High Dielectric Constant in Al2O3/TiO2 Nanolaminates Grown by Pulsed Laser Deposition, ACS Appl. Mater. Interfaces 14 (2022) 12873–12882. https://doi.org/10.1021/ACSAMI.1C25028.

[51] A.K. Jonscher, Frequency-dependence of conductivity in hopping systems, J. Non. Cryst. Solids 8–10 (1972) 293–315. https://doi.org/10.1016/0022-3093(72)90151-2.

[52] Y. Guo, R.M. Bustin, Micro-FTIR spectroscopy of liptinite macerals in coal, Int. J. Coal Geol. 36 (1998) 259–275. https://doi.org/10.1016/S0166-5162(97)00044-X.

[53] M. Ashokkumar, S. Muthukumaran, Microstructure, optical and FTIR studies of Ni, Cu co-doped ZnO nanoparticles by co-precipitation method, Opt. Mater. (Amst). 37 (2014) 671–678. https://doi.org/10.1016/J.OPTMAT.2014.08.012.

[54] D.S. Gandolfo, H. Mortimer, J.W. Woodhall, N. Boonham, Fourier transform infra-red spectroscopy using an attenuated total reflection probe to distinguish between Japanese larch, pine and citrus plants in healthy and diseased states, Spectrochim. Acta A Mol. Biomol. Spectrosc. 163 (2016) 181–188. https://doi.org/10.1016/J.SAA.2016.03.022.

[55] M. Pantelidou, P.R. Chitnis, J. Breton, FTIR Spectroscopy of Synechocystis 6803 Mutants Affected on the Hydrogen Bonds to the Carbonyl Groups of the PsaA Chlorophyll of P700 Supports an Extensive Delocalization of the Charge in P700+†, Biochemistry 43 (2004) 8380–8390. https://doi.org/10.1021/BI049515J.

[56] A. Alam, Mst.S. Akter, S. Akter, Md.R. Hasan, Md.A. Rob, J. Maudood, Md.S. Islam, N. Khatun, S. Islam, A.K. Azad, Md.S. Alam, S. Hossain, Cr-site engineering of BaFeO3 perovskites: correlating structural defects, electronic structure, optical response and charge transport, Journal of Materials Science: Materials in Electronics 2026 37:28 37 (2026) 2167-. https://doi.org/10.1007/S10854-026-18526-9.

Supplementary Files

This is a list of supplementary files associated with this preprint. Click to download.

- GraphicalAbstract.png